15328 *J. Phys. Chem. A* **2009,** *113,* 15328–15345

Crossed-Beam Dynamics, Low-Temperature Kinetics, and Theoretical Studies of the Reaction $S(^1D) + C_2H_4$[†]

Francesca Leonori, Raffaele Petrucci, Nadia Balucani, and Piergiorgio Casavecchia*

Dipartimento di Chimica, Università degli Studi di Perugia, 06123 Perugia. Italy

Marzio Rosi

Dipartimento di Ingegneria Civile e Ambientale and ISTM-CNR, c/o Dipartimento di Chimica, Università degli Studi di Perugia, 06123 Perugia, Italy

Dimitris Skouteris

Dipartimento di Matematica e Informatica and Dipartimento di Chimica, Università degli Studi di Perugia, 06123 Perugia, Italy

Coralie Berteloite, Sébastien D. Le Picard, André Canosa, and Ian R. Sims*

Institut de Physique de Rennes, Equipe Astrochimie Expérimentale, UMR 6251 du CNRS−Université de Rennes 1, Bât. 11c, Campus de Beaulieu, 35042 Rennes Cedex, France

Received: July 3, 2009; Revised Manuscript Received: August 25, 2009

The reaction between sulfur atoms in the first electronically excited state, $S(^1D)$, and ethene (C_2H_4) has been investigated in a complementary fashion in (a) crossed-beam dynamic experiments with mass spectrometric detection and time-of-flight (TOF) analysis at two collision energies (37.0 and 45.0 kJ mol^{-1}), (b) low temperature kinetics experiments ranging from 298 K down to 23 K, and (c) electronic structure calculations of stationary points and product energetics on the C_2H_4S singlet and triplet potential energy surfaces. The rate coefficients for total loss of $S(^1D)$ are found to be very large (ca. 4×10^{-10} cm^3 molecule^{-1} s^{-1}) down to very low temperatures indicating that the overall reaction is barrierless. From laboratory angular and TOF distributions at different product masses, three competing reaction channels leading to $H + CH_2CHS$ (thiovinoxy), $H_2 + CH_2CS$ (thioketene), and $CH_3 + HCS$ (thioformyl) have been unambiguously identified and their dynamics characterized. Product branching ratios have also been estimated. Interpretation of the experimental results on the reaction kinetics and dynamics is assisted by high-level theoretical calculations on the C_2H_4S singlet potential energy surface. RRKM (Rice−Ramsperger−Kassel−Marcus) estimates of the product branching ratios using the newly developed singlet potential energy surface have also been performed and compared with the experimental determinations.

1. Introduction

The elementary reactions of atomic sulfur with inorganic and organic compounds are of interest in different areas, such as material sciences (especially in the production of sulfur-doped diamond[1−3]), combustion of S-containing fuel and coal,[4] atmospheric chemistry,[5] and astrochemistry.[6−10] Simple organo-sulfur molecules or radicals have been observed in these environments, raising the question of how they are formed under such different conditions. Quite interestingly, the combustion of sulfur-rich fuels generates more soot than the sulfur-poor ones[11] and the formation of the CS radical in the gas phase is considered to be the first step of sulfur incorporation into the diamond structure.[2] Nevertheless, the scarcity of experimental data, especially at the most detailed level of reaction dynamics studies, has impeded so far an assessment of the role played by the reactions of atomic sulfur or other transient sulfur species, such as S_2, with hydrocarbons or hydrocarbon radicals in all of the above-mentioned environments.

Pioneering kinetics[12,13] and theoretical work[14,15] on reactions of ground and excited state sulfur atoms, $S(^3P,^1D)$, with hydrocarbons has shown that, similarly to the case of $O(^1D)$ with respect to $O(^3P)$, atomic sulfur in the first electronically excited state ^1D (located 110.5 kJ mol^{-1} above the ground state[16]) is much more reactive than atoms in the ground ^3P state. More recent kinetics work, in which the rate coefficients for $S(^1D)$ removal from several species at 300 K have been measured and compared with those of the related species $O(^1D)$,[17] has indicated that the rate coefficients are very high and similar in the two cases. In this respect, it should be noted that, as for the case of several $O(^1D)$ reactions, the reactions of $S(^1D)$ may also be of relevance in atmospheric chemistry. In fact, several reduced sulfur compounds are abundantly released on the terrestrial surface from biogenic sources. Such reduced sulfur compounds are partly converted to carbonyl sulfide (OCS), the most abundant atmospheric sulfur species.[18] OCS is a relatively inert species that reaches the upper troposphere.[18] There, OCS can photodissociate in the window between the O_2 and O_3 absorptions and produce CO and $S(^3P,^1D)$, with the spin-allowed production of $S(^1D)$ being the dominant channel.[19] Other

---

[†] Part of the “Vincenzo Aquilanti Festschrift”.

* Corresponding authors, piero@dyn.unipg.it and ian.sims@univ-rennes1.fr.

10.1021/jp906299v

reduced sulfur compounds can also be injected directly into the stratosphere by volcanic eruption[20] and their photodissociation can be a source of $S(^3P,^1D)$. For instance, the photodissociation of H_2S at the Lyman-α wavelength can occur via a three-body dissociation with $S(^1D)$ formation[21] and the SH radical photodissociation can generate $S(^1D)$ in addition to $S(^3P)$. Since the lifetime of the metastable excited state is relatively long (28 s),[16] $S(^1D)$ will react with atmospheric constituents or undergo physical quenching. Nevertheless, the role of $S(^1D)$ production at the troposphere−stratosphere border and in the stratosphere has not been clarified yet.

In addition to atmospheric chemistry, $S(^1D)$ reactions with simple hydrocarbons can be of relevance in the chemical vapor deposition processes that exploit plasma production by microwave or radio frequency discharge, as electrical discharges in H_2S may produce also $S(^1D)$ and the more pronounced reactivity of $S(^1D)$ with respect to ground state sulfur atoms can make its role more important than it is currently believed.[1a] Notably, the only previous reaction dynamics studies of S-atoms have been carried out on two reactions of $S(^1D)$: Liu and co-workers have investigated the reaction $S(^1D) + H_2$ (HD,D_2) by using a pulsed CMB apparatus with REMPI detection of the H product within a Doppler-shift scheme,[22] while Dagdigian and co-workers performed laser-induced fluorescence (LIF) studies of the SD product rotational distribution from the $S(^1D) + D_2$ and $S(^1D) + CD_4$ reactions[23,24] in a photolysis-probe experiment.

Since for sulfur reactions with hydrocarbons (alkanes, alkenes, and alkynes) there is a limited amount of kinetics work, mostly at room temperature, and, with the exception of the LIF study on $S(^1D) + CH_4$ reaction, no dynamics studies, we have recently undertaken a systematic investigation of $S(^1D)$ reactions with hydrocarbons. In particular, we have investigated the reaction dynamics of $S(^1D) + C_2H_2$, C_2H_4, and CH_4 by means of the crossed molecular beam (CMB) scattering technique with "universal" mass spectrometric (MS) detection[25−27] and established the nature of the products and their branching ratios. In addition, to enlarge the temperature range of kinetics measurements and to explore the details of the entrance channel of the underlying potential energy surface (PES), the determinations of the rate coefficients for $S(^1D)$ removal with a variety of hydrocarbons in a CRESU (Cinétique de Réaction en Ecoulement Supersonique Uniforme, or Reaction Kinetics in Uniform Supersonic Flow) apparatus, from room temperature down to about 20 K, has been pursued by some of the present authors.[26,27] Finally, to assist the interpretation of the experimental results and characterize the minimum energy path, the experimental effort has been empowered by high-level electronic structure calculations of the relevant PESs at B3LYP and CCSD(T) levels of theory, with thermochemical calculations also performed at the W1 level.[25−27] A combined crossed-beam and theoretical study of the $S(^1D) + C_2H_2$ reaction has been published very recently,[25] a preliminary communication on the combined crossed-beam, kinetics, and theoretical investigation of the title reaction has been reported,[26] while a report on a combined experimental (kinetics and dynamics) and theoretical study of $S(^1D) + CH_4$ is in preparation.[27]

In contrast to $S(^1D) + C_2H_2$ for which only one reaction channel, that leading to HCCS + H, was found to be open,[25] in the case of the $S(^1D) + C_2H_4$ reaction three competing reaction channels leading to thiovinoxy, thioketene and thioformyl have been observed in CMB-MS experiments.[26] As a matter of fact, according to our theoretical calculations,[26] the possible reaction channels within the range of collision energy of this study are numerous

$$S(^1D) + C_2H_4(X^1A_g) \rightarrow CH_2CHS(X^2A'') + H(^2S) \tag{1}$$

$$\Delta H_0^\circ = -26.2 \text{ kJ mol}^{-1}$$

$$S(^1D) + C_2H_4(X^1A_g) \rightarrow CH_3CS(X^2A') + H(^2S) \tag{2}$$

$$\Delta H_0^\circ = +12.4 \text{ kJ mol}^{-1}$$

$$S(^1D) + C_2H_4(X^1A_g) \rightarrow CH_2CS(X^1A_1) + H_2(X^1\Sigma_g) \tag{3}$$

$$\Delta H_0^\circ = -244.6 \text{ kJ mol}^{-1}$$

$$S(^1D) + C_2H_4(X^1A_g) \rightarrow HCS(X^2A') + CH_3(X^2A_2'') \tag{4}$$

$$\Delta H_0^\circ = -9.1 \text{ kJ mol}^{-1}$$

$$S(^1D) + C_2H_4(X^1A_g) \rightarrow HS(X^2\Pi) + C_2H_3(X^2A') \tag{5}$$

$$\Delta H_0^\circ = -5.2 \text{ kJ mol}^{-1}$$

$$S(^1D) + C_2H_4(X^1A_g) \rightarrow CS(X^1\Sigma^+) + CH_4(X^1A_1) \tag{6}$$

$$\Delta H_0^\circ = -233.7 \text{ kJ mol}^{-1}$$

The above reaction enthalpies are those calculated at the W1 level of theory.[26]

The rate coefficient for $S(^1D)$ removal (reaction and quenching) by ethene was determined to be 4.1×10^{-10} cm^3 molecule^{-1} s^{-1} at 300 K by Black and Jusinski.[17] This large value has been confirmed by our recent CRESU experiments, which also showed that there is essentially no dependence of the rate coefficients on temperature and that the reaction remains very rapid down to the lowest temperature of 23 K.[26] Black[28] also studied the branching ratio between physical quenching and reaction and found that the $S(^1D) + C_2H_4$ interaction is dominated by quenching (with a branching fraction of 0.77 ± 0.05), reaction only accounting for about one-quarter (0.23 ± 0.05) of the total rate. This fraction is higher than a previous estimate (0.48) by Gunning and co-workers (quoted in ref 28). According to these results, therefore, intersystem-crossing (ISC) from triplet to singlet PESs occurs readily. Those studies, however, were not able to discriminate among the possible reaction products. This is indeed the current status for most $S(^3P,^1D)$ reactions with hydrocarbons.

In this paper, we complement the preliminary communication of ref 26 by reporting (i) the complete set of experimental data and best-fit functions for the CMB experiment at the collision energy E_c of 37.0 kJ mol^{-1} and the new results obtained at a slightly higher E_c of 45.0 kJ mol^{-1}; (ii) the complete set of kinetics data from room temperature down to 23 K; (iii) the details of the electronic structure calculations of the singlet PES anticipated in the previous communication[26] and the electronic structure calculations for the triplet C_2H_4S PES, which can be involved in the reaction if ISC from the singlet to the triplet PESs takes place; (iv) RRKM estimates of the product branching ratios performed on the calculated singlet PES.

The paper is organized as follows. In section 2 we describe the kinetics and crossed-beam experiments. In section 3 computational details on electronic structure as well as RRKM calculations are provided. The experimental and theoretical results are presented in section 4. Discussion follows in section 5 and conclusions are given in section 6.

2. Experimental Section

2.1. Low-Temperature Rate Coefficient Measurements. Rate coefficients for the removal of $S(^1D)$ atoms by C_2H_4 were obtained using the CRESU apparatus in Rennes, combined with the pulsed-laser photolysis−laser-induced fluorescence (PLP-LIF) technique. Since the apparatus has been described elsewhere,[29,30] only a brief overview will be given here, focusing on the experimental details relevant to the study of the kinetics of $S(^1D)$.

The CRESU technique is based on a buffer gas isentropic expansion through a Laval nozzle, generating cold supersonic flows of relatively high density ($10^{16}-10^{17}$ cm^{-3}). As a result, molecular collisions are frequent and thermal equilibrium is maintained for several tens of centimeters, corresponding to some hundreds of microseconds, downstream of the nozzle exit. Buffer (He) and reagent (C_2H_4) gases were used directly from their cylinders and mixed before their injection in the reservoir. Both gases were furnished by Air Liquide, helium with a stated purity of 99.995% and C_2H_4 with a stated purity of 99.95%. Flows of carrier and reagent gases were regulated by means of independently calibrated MKS mass flow controllers. Knowledge of the total gas density along the flow, achieved by means of impact pressure measurements, and of each gas flow rate, enabled the calculation of the concentration of the reactants in the supersonic expansion.

$S(^1D)$ atoms were produced, coaxially to the flow, by PLP of carbon disulfide (CS_2) which was injected at very low concentration directly into the reservoir via a separate Teflon precursor line. Photolysis was accomplished at 193 nm using the unfocused beam of an ArF excimer laser (Lambda Physics, LPX 210i, 10 Hz). The photolysis laser fluence used was ca. 50 mJ cm^{-2} in the reaction zone with a ca. 25 ns full width at half-maximum pulse. Photolysis of CS_2 (193 nm) has been studied by a number of groups,[31] and there has been some disagreement over the branching ratio $S(^3P)/S(^1D)$. Kitsopoulos et al., while measuring a value of 1.5 ± 0.4 for this ratio, note that the average measured value (across different experimental studies) is about 3 ± 2.[32] The estimated flow rate of CS_2 was ca. 0.1 sccm (standard cm^3 min^{-1}), yielding under these conditions a concentration of $S(^1D)$ of ca. 2×10^{10} cm^{-3}, thus avoiding any problems with self- or cross-reactions, and meeting so-called pseudo-first-order conditions for the measurement of the rate coefficients. The only major side reaction could be that between $S(^1D)$ atoms and CS_2 precursor, and the contribution of this reaction to the measured first-order rate coefficients was constant for a given set of measurements on a single hydrocarbon coreagent, thus having no systematic influence on the measured second-order rate coefficients. Furthermore, quenching by the He buffer gas is likely to exceed this reactive contribution. Measurements on quenching of $S(^1D)$ by Ar and N_2 made in the CRESU apparatus show that these processes are very rapid, precluding their use as buffer gases.[33] However, quenching by He was found to be slow enough to allow kinetics measurements to be made on the removal of $S(^1D)$ by a variety of collision partners.

Detection of $S(^1D)$ atoms was achieved by resonant one-photon vacuum ultraviolet laser-induced fluorescence (VUV LIF) at 166.67 nm, on the $3s^23p^4-3s^23p^3(^2D°)4s$ transition. VUV laser radiation was generated by two-photon resonant four-wave frequency mixing in xenon,[34] in a similar way to previous work involving VUV LIF detection of $C(^3P)$.[35] Around 2 mbar of Xe was used in the frequency mixing cell. Two tunable dye laser pulses were used: the first was the frequency-doubled output of a 355 nm Nd:YAG-pumped dye laser (LAS, LDL 205) at ca. 256 nm with an energy of ca. 2 mJ, and it excited the Xe $5p^56p[21/2, 2]$ state via a two-photon transition. Excitation of this resonance was ensured by monitoring the Xe^+ multiphoton ionization signal in a separate cell. Another, visible dye laser beam (pulse energy ∼20 mJ) at a wavelength of around 552 nm was generated in a second dye laser (Continuum ND6000, using Exciton Rhodamine 590 or Pyrromethene 580 dye) pumped by the same Nd:YAG laser (Continuum Precision II), but at 532 nm, and combined and copropagated into the Xe cell, generating VUV radiation at 166.67 nm. The resultant VUV beam intersected the CRESU flow and the photolysis beam at the focus of an optically fast CaF_2 condenser lens pair, which imaged any resulting fluorescence onto the photocathode of a VUV solar blind photomultiplier tube (Electron Tubes, type 9403) after passing through a VUV interference filter (Acton Research) centered at 159.8 nm (23.4 nm bandwidth). Subsequent signal acquisition was performed as in previous studies,[32] and the experiment was controlled by data acquisition software coded in-house using National Instruments Labview. The LIF decays comprised 200 points and were averaged for a total of eight laser shots per point in repeated scans. Two typical decay traces for $S(^1D)$ atomic fluorescence in the presence of ethene, C_2H_4, at 23 and 49 K are illustrated in Figure 1. The observed single-exponential decays confirm that the experiment was performed under pseudo-first-order conditions. Decays were recorded for a range of differing ethene concentrations and fitted to single exponential decay functions to yield pseudo-first-order rate coefficients. These were then plotted against ethene concentration to yield so-called second-order plots, the gradients of which correspond to the measured second-order rate coefficients. Two examples of second-order plots at 23 and 49 K can also be seen in Figure 1, demonstrating the excellent linearity and signal-to-noise achieved in these experiments.

2.2. Crossed-Beam Measurements. The reactive scattering experiments were performed at two collision energies, E_c, of 37.0 and 45.0 kJ mol^{-1} using the Perugia "universal" CMB apparatus which has been described elsewhere.[36,37] Briefly, two well-collimated, in angle and velocity, continuous supersonic beams of the reactants are crossed at 90° in a large scattering chamber maintained at a pressure of 2×10^{-6} hPa while operating. The angular and velocity distributions of the products are measured by a ultrahigh vacuum (10^{-11} hPa) rotatable quadrupole mass spectrometer detector equipped with a tunable electron-impact ionizer. Continuous supersonic beams of $S(^3P, {}^1D)$ atoms are generated from a high-pressure, high-power radio frequency (rf) discharge beam source[38] which has been successfully used in our laboratory to produce other atomic and molecular radicals.[36,39] For the production of atomic sulfur we use SO_2 as molecular precursor and we have obtained experimental evidence[25] that the sulfur atoms are produced not only in the ground electronic state, ^3P, but also in the first excited, metastable state ^1D. By discharging 65 hPa of a 1% SO_2 in

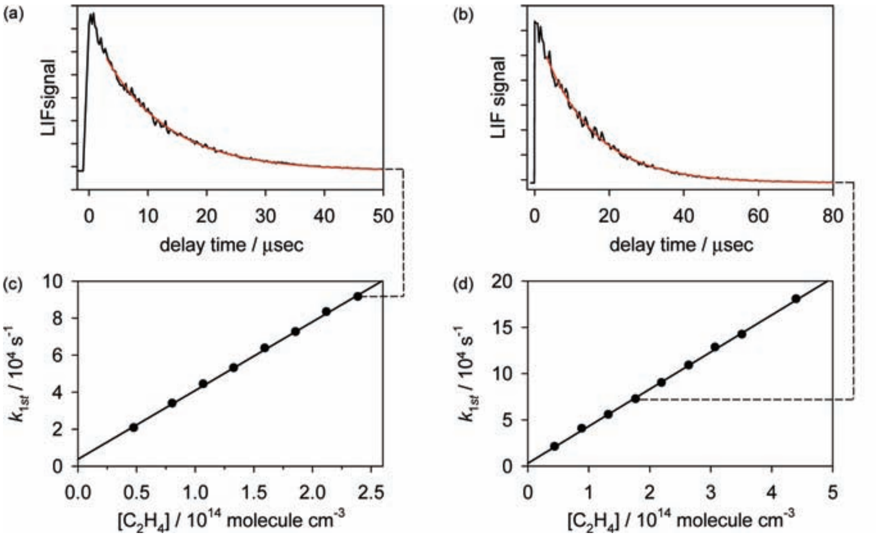

Figure 1. The upper panels show the fitted decays of the S(^{1}D) laser-induced fluorescence observed in mixtures containing (a) 2.39 × 10^{14} molecules cm^{-3} C_2H_4 at 23 K and (b) 1.77 × 10^{14} molecules cm^{-3} C_2H_4 at 49 K. The lower panels show plots of the pseudo-first-order rate coefficients obtained from such experiments plotted against the concentration of C_2H_4 at (c) 23 K and (d) 49 K.

helium gas mixture through a 0.55 mm diameter quartz nozzle at 300 W of nominal rf power, a supersonic beam with a peak velocity of 2067 m s^{-1} and a speed ratio of 5.7 was obtained. Supersonic beams of ethene having different velocity were generated by expanding through a 100 μm diameter stainless-steel nozzle kept at room temperature 750 hPa of neat C_2H_4 (beam peak velocity 823 m s^{-1}; speed ratio 5.8) and 750 hPa of a 18% C_2H_4 in H_2 gas mixture (peak velocity 1444 m s^{-1}; speed ratio 12.6). Under these expansion conditions C_2H_4 clustering was negligible. Because of the significant cooling during supersonic expansion, the ethene molecules in the beam are expected to be in the lowest rotational states of the ground vibrational level, and therefore the internal energy of the molecular reactant contributes negligibly to the total available energy. The ensuing collision energies were 37.0 and 45.0 kJ mol^{-1}, respectively. The C_2H_4 beam was modulated at 160 Hz by a tuning-fork chopper for background subtraction. Velocity analysis of the beams was carried out by conventional "single-shot" time-of-flight (TOF) techniques.[37] Velocity distributions of the products were obtained at selected laboratory angles using the cross-correlation TOF method[34] with a dwell time of 6 μs/channel. The flight length was 24.3 cm. Counting times varied from 45 to 240 min depending upon the signal intensity.

3. Computational Details

3.1. Electronic Structure Calculations. The potential energy surface of the system S(^{1}D, ^{3}P) + C_2H_4 was investigated localizing the lowest stationary points at the B3LYP[40] level of theory in conjunction with the correlation consistent valence polarized set aug-cc-pVTZ,[41] augmented with a tight *d* function with exponent 2.457 for the sulfur atoms[42] to correct for the core polarization effects.[43] This basis set will be denoted aug-cc-pV(T+*d*)Z. At the same level of theory we have computed the harmonic vibrational frequencies in order to check the nature of the stationary points, i.e., minimum if all the frequencies are real, saddle point if there is one, and only one, imaginary frequency. The assignment of the saddle points was performed using intrinsic reaction coordinate (IRC) calculations.[44] The energy of all the stationary points was computed at the higher level of calculation CCSD(T)[45] using the same basis set aug-cc-pV(T+*d*)Z. Both the B3LYP and the CCSD(T) energies were corrected to 0 K by adding the zero point energy correction computed using the scaled harmonic vibrational frequencies evaluated at B3LYP/aug-cc-pV(T+*d*)Z level. The energy of S(^{1}D) was estimated by adding the experimental[16,46] separation S(^{3}P)−S(^{1}D) of 110.5 kJ mol^{-1} to the energy of S(^{3}P) at all levels of calculation. Thermochemical calculations were performed at the W1[47] level of theory for selected points. We note that in the W1 method[47] the geometry optimization and the evaluation of the frequencies are performed at the B3LYP/VTZ + *d* level while the energies are computed at the CCSD(T)/AVDZ + 2*d*, CCSD(T)/AVTZ + 2*d*1*f*, CCSD/AVQZ + 2*d*1*f* level of theory (AV*n*Z is for aug-cc-pV*n*Z with n = D, T, Q). All calculations were performed using Gaussian 03[48] while the analysis of the vibrational frequencies was performed using Molekel.[49]

3.2. RRKM Calculations. We have performed RRKM (Rice−Ramsperger−Kassel−Marcus) calculations on the S(^{1}D) + C_2H_4 system, using a code developed for this purpose.[50] In accordance with the RRKM scheme,[51] the microcanonical rate constant for a specific reaction at a specific total energy (hereby denoted by $k(E)$) is given by the expression

$$k(E) = \frac{N_{\mathrm{TS}}(E)}{\rho_{\mathrm{r}}(E)}$$

where $N_{\mathrm{TS}}(E)$ stands for the number of states (orthogonal to the reaction coordinate) open at the transition state at an energy E, and $\rho_{\mathrm{r}}(E)$ denotes the reactant density of states at the same energy. Regarding the total angular momentum (J), the system was assumed to be described by a distribution of J states between 0 and 50, where each value of J is weighted by a factor proportional to its corresponding density of states at the energy concerned. We have noted that, even though the J distribution can influence considerably the absolute value of the rate constants, it only has a minimal effect on the branching ratios.

The rotational densities of states, both for the reactants and for the transition states, were calculated using an inverse Laplace transform of the corresponding partition functions. Subsequently, the rotational densities of states were convoluted with the corresponding vibrational ones using a direct count algorithm. Finally, the density of states for the transition state was appropriately integrated with respect to the energy in order to

TABLE 1: Rate Coefficients k for the Removal of $S(^1D)$ by Ethene (by Reaction and Relaxation)

T/K	[He]/10^{16} molecules cm^{-3}	$[C_2H_4]/10^{13}$ molecules cm^{-3}	no. of points	k /10^{-10} cm^3 $molecule^{-1}$ s^{-1}
23	4.73	4.8 − 23.9	8	3.71 ± 0.39[a]
49	10.4	4.5 − 44.0	9	4.01 ± 0.41
123	12.7	0.06 − 7.1	10	5.02 ± 0.51
298	29.2	1.3 − 40.6	11	4.51 ± 0.46

[a] Uncertainties are calculated using the standard error evaluated from the second-order plot, multiplied by the appropriate Student's *t* factor for 95% confidence. A systematic error of 10% was combined with this to take into account the contribution from possible systematic error (see text for further details).

produce the sum of states required. Tunneling contributions were included in all cases where a "stiff" transition state was involved, using an Eckart barrier simulation with the appropriate imaginary frequency. These were found, in all cases, to make no important contribution to the rate constants.

In the cases of "loose" transition states (monotonic dissociation channels), we performed ab initio and RRKM calculations at various points along the dissociation coordinate, choosing as a transition state the point yielding the minimum value of the rate constant in accordance with the variational (VTST) approach.[52] The vibrational frequencies and rotational constants derived from the constrained optimization at the intermediate points were used as inputs in the RRKM calculations.

4. Results and Discussion

4.1. Kinetics Results. The measured rate coefficients over the temperature range 23—298 K are displayed in Table 1. For each measurement, the main flow conditions (buffer gas, total density, range of reactant gas density) are noted, as well as the number of experimental points used in the second-order plots. Quoted uncertainties include both statistical and systematic errors and are evaluated as the square root of the sum of these two independent errors squared. Statistical errors are calculated as the standard error from the unweighted fit of the second order plot multiplied by the appropriate Student's *t* factor (depending upon the number of experimental points in the second order plot) for the 95% confidence limit. Systematic errors were more difficult to estimate but are likely to arise from inaccuracies in the calibration of the flow controllers, affecting the determination of the buffer and reactant densities. Every effort was made to minimize these systematic errors, and we estimate that they do not exceed 10%.

The measured rate coefficients for the removal of $S(^1D)$ by C_2H_4 are plotted as a function of temperature on a log−log scale in Figure 2, along with the room temperature result of Black and Jusinski.[17] Agreement is excellent with the latter, and the rate coefficients show hardly any dependence on temperature, remaining very rapid down to the lowest temperature at which measurements were performed, 23 K. A fit to a modified Arrhenius-type function of the form $k(T) = A(T/298\ K)^n \exp(\theta/T)$ yields $A = 4.81 \times 10^{-10}$ cm^3 $molecule^{-1}$ s^{-1}, $n = 0.049$ and $\theta = -9.6$ K, with a root-mean-square deviation of the experimental points from this fit of 2.6×10^{-11} cm^3 $molecule^{-1}$ s^{-1}. The mean value of the rate coefficient over the measured temperature range is $(4.2^{+0.8}_{-0.5}) \times 10^{-10}$ cm^3 $molecule^{-1}$ s^{-1}.

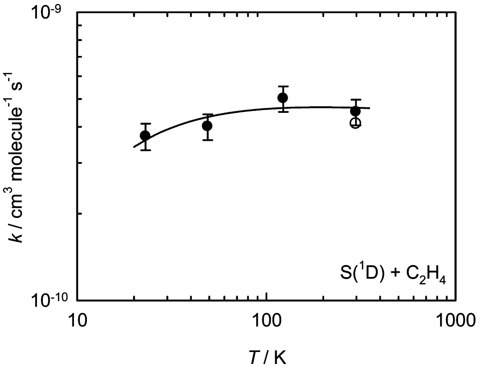

Figure 2. Rate coefficients $k(T)$ for the total removal of $S(^1D)$ atoms by C_2H_4 as a function of temperature, displayed on a log−log scale. The solid symbols show the results of this study, while the open circle shows the room temperature result of Black and Jusinski.[17] The solid line shows the result of a fit to an equation of the form $k(T) = A(T/298\ K)^n \exp(\theta/T)$ yielding $A = 4.81 \times 10^{-10}$ cm^3 $molecule^{-1}$ s^{-1}, $n = 0.049$ and $\theta = -9.6$ K. The root-mean-square deviation of the experimental points from this fit is 2.6×10^{-11} cm^3 $molecule^{-1}$ s^{-1}. The mean value of the rate coefficient over the measured temperature range is $(4.2^{+0.8}_{-0.5}) \times 10^{-10}$ cm^3 $molecule^{-1}$ s^{-1}.

4.2. Crossed-Beam Results. Product laboratory (LAB) angular distributions, $N(\Theta)$, were recorded at the mass-to-charge ratios $m/z = 59$ ($C_2H_3S^+$), $m/z = 58$ ($C_2H_2S^+$), and $m/z = 45$ (HCS^+) by counting for 100 s at each angle and averaging over at least four scans. Figures 3 and 4 show the $m/z = 59$, $m/z = 58$, and $m/z = 45$ $N(\Theta)$ together with the velocity vector (Newton) diagram of the experiment at $E_c = 37.0$ kJ mol^{-1} and $E_c = 45.0$ kJ mol^{-1}, respectively. As can be seen the $N(\Theta)$ at the parent mass of CH_2CHS ($m/z = 59$) (top panels in Figures 3 and 4) is very narrow reflecting the formation of a heavy coproduct confined around the center-of-mass (CM), left by a light H-atom (channel 1), and a small reaction exoergicity. In contrast, the $m/z = 45$ $N(\Theta)$ (bottom panels in Figures 3 and 4) extends over a much wider angular range reflecting the formation of HCS from channel (4), left by the sizable CH_3 cofragment. The $m/z = 45$ $N(\Theta)$ also exhibits a clear peak centered at the CM angle, which can be readily attributed to dissociative ionization of the CH_2CHS product from channel (1) in the electron impact ionizer. These two contributions are confirmed and disentangled by TOF measurements at selected LAB angles for $m/z = 59$ and 45, as shown in Figures 5 and 6 for the low E_c and high E_c, respectively. As can be clearly seen the $m/z = 59$ TOF spectra (left panels in Figures 5 and 6) exhibit a single peak which reflects the velocity distribution of the sole CH_2CHS product from channel (1). In contrast, the $m/z = 45$ spectra (right panels in Figures 5 and 6) exhibit clearly a two peak structure, in which the slower peak has the same position as that recorded at $m/z = 59$ and clearly originates from the dissociative ionization to $m/z = 45$ of the CH_2CHS product, and the faster peak is unambiguously attributed, on the basis of energy and momentum conservation, to the HCS product parent ion from channel (4).

The $m/z = 58$ $N(\Theta)$s (middle panels in Figures 3 and 4) resemble closely the $m/z = 59$ $N(\Theta)$s, reflecting a significant dissociative ionization of the CH_2CHS product, but they also exhibit a significantly higher intensity on the wings (this is especially visible at large angles) which is attributed to the parent ion of the CH_2CS product from the H_2 elimination channel (3). This is confirmed by the TOF distributions measured at $m/z = 58$ (see central panels in Figures 5 and 6). As can be seen, the $m/z = 58$ spectra resemble very closely those measured at m/z

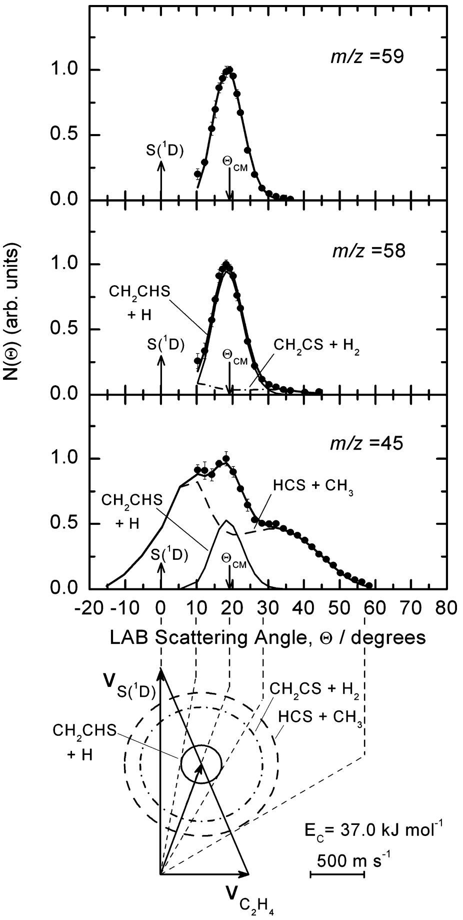

Figure 3. LAB angular distribution, $N(\Theta)$, of (top panel) $m/z = 59$ product (CH_2CHS) (solid circles), (middle panel) $m/z = 58$ products (CH_2CHS and CH_2CS) (solid circles), (bottom panel) $m/z = 45$ products (CH_2CHS and HCS) (solid circles) from the reactions $S(^1D) + C_2H_4$ at $E_c = 37.0$ kJ mol^{-1}, together with the velocity vector diagram of the experiment. Error bars, when visible outside the dots, represent ±1 standard deviation from the mean. The circles in the Newton diagram delimit the maximum velocity that the CH_2CHS, CH_2CS, and HCS products from channels (1), (3), and (4), respectively, can attain if all the available energy is channeled into product translational energy. The solid line is the total $N(\Theta)$ calculated when using the best-fit CM angular and translational energy distributions; at $m/z = 58$ and 45 the separated contributions of channels (1) and (3), and channels (4) and (1), respectively, are indicated.

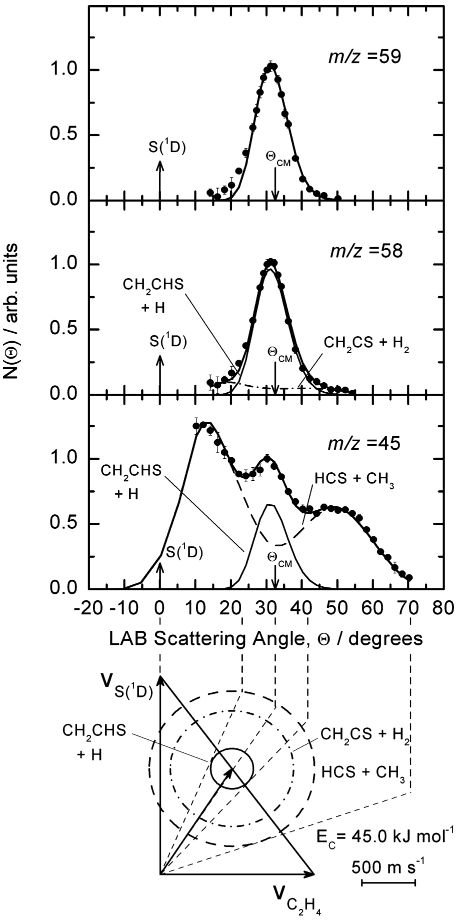

Figure 4. As in Figure 3, but at $E_c = 45.0$ kJ mol^{-1}.

= 59, but they also exhibit a small, faster shoulder which is attributed, on the basis of energy and linear momentum conservation, to the CH_2CS product from channel (3). This fast shoulder is discernible only at large angles where the relative weight of the H_2 channel is largest (see, for instance, the TOF spectra at $\Theta = 24°$ and 30° at low E_c in Figure 5 and at $\Theta = 40°$ at high E_c in Figure 6).

The fit of the LAB data is performed by a forward convolution procedure which employs tentative CM angular, $T(\theta)$, and translational energy, $P(E'_T)$, distributions for the various product channels, weighted according to their relative contributions. In the forward convolution trial and error fitting procedure the CM product flux was expressed according to

$$I_{CM}(\theta, E'_T) = \sum_i w_i T(\theta)_i P(E'_T)_i \tag{7}$$

where $T(\theta)_i$ and $P(E'_T)_i$ are the CM angular and translational energy distributions of the ith reaction channel, and the coefficient w_i the relative weight of the apparent cross section for the ith contribution. In the best-fit of the $m/z = 58$ data, where the H channel (reaction 1) and the H_2 channel (reaction 3) contribute, the w_H and w_{H2} values are 0.54 and 0.46 at $E_c = 37.0$ kJ mol^{-1} and 0.56 and 0.44 at $E_c = 45.0$ kJ mol^{-1}. In the best-fit of the $m/z = 45$ data, where the H channel and the HCS channel (reaction 4) contribute, the w_H and w_{HCS} values are 0.053 and 0.947 at $E_c = 37.0$ kJ mol^{-1} and 0.045 and 0.955 at $E_c = 45.0$ kJ mol^{-1}.

In the Figures 3−6 the heavy solid curves represent the global best-fit of the experimental data according to eq 7 with the above best-fit w_i values, while the light-solid, the dashed-dotted, and the dashed lines represent the contributions of the $CH_2CHS + H$, $CH_2CS + H_2$, and $HCS + CH_3$ channels, respectively. The best-fit $T(\theta)$ and $P(E'_T)$, distributions for the indicated three competing channels are reported in Figures 7 and 8 for the low and high E_c experiment, respectively. As can be seen, the best-fit $T(\theta)$s for all three channels exhibit significant intensity in the whole CM angular range, with a marked preference for the forward direction (with respect to the S-atom direction). This is consistent, within the *osculating* model of chemical reactions,[53] with the formation of a bound intermediate having a lifetime comparable to its rotational period. The detailed shape of the $T(\theta)$ as well as of the $P(E'_T)$ distributions is however quite different for the three channels, reflecting the topology (presence or not of an exit potential barrier, for instance) of the singlet PES shown in Figure 10. In particular, in the case of channel (4), the $P(E'_T)$ and $T(\theta)$ functions are strongly coupled, as can be seen from the bottom panels in the right-hand side of Figures 7 and 8, that is, the fraction of energy released into product recoil energy varies with the recoil direction.

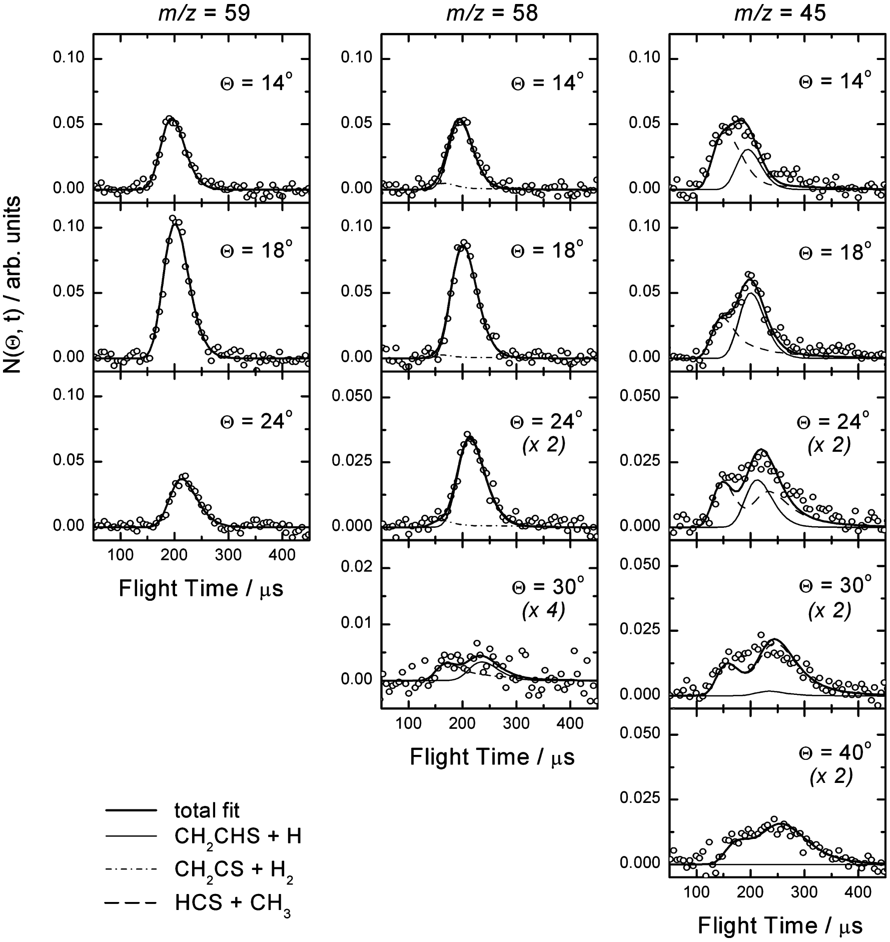

Figure 5. Time-of-flight distributions at the indicated LAB angles of the products at $m/z = 59$ (left panels), $m/z = 58$ (central panels), and $m/z = 45$ (right panels) for $E_c = 37.0$ kJ mol^{-1}. For $m/z = 58$ the TOF spectra at $\Theta = 24°$ and 30° are amplified by factors 2 and 4, respectively, for clarity. For $m/z = 45$ the TOF spectra at $\Theta = 24°$, 30°, and 40° are also amplified by a factor 2 for clarity. The various lines (symbols as in the legend) are the calculated distributions from the indicated contributing channels using the best-fit CM functions.

The $T(\theta)$ for the CH_2CHS product exhibits an asymmetry ratio between the backward ($\theta = 180°$) and the forward ($\theta = 0°$) directions of 0.3 at low E_c and 0.15 at high E_c, consistent with the trend that one would expect on the basis of the osculating complex model, but it also exhibits a large intensity in the sideways direction, that is, the $T(\theta)$ is not polarized. The $T(\theta)$ for the CH_2CS product is strongly forward peaked with a uniform intensity in the sideways and backward directions; within the experimental sensitivity the $T(\theta)$ is identical at the two similar E_cs. For these two channels the uncertainty in the backward to forward ratio is ±0.10.

The $T(\theta)$ for the HCS channel is strongly polarized and exhibits a marked asymmetry similar to that of the H channel, although somewhat less pronounced. In fact, the $T(180°)/T(0°)$ ratio is 0.634 at low E_c and 0.385 at high E_c. This reflects, within the osculating complex model, a slightly longer complex lifetime with respect to the H channel. What is remarkable for the HCS channel is the strong polarization of the $T(\theta)$ with an intensity ratio $T(90°)/T(0°)$ of 0.11 at both E_cs. This polarization reflects a quite different partitioning of the total angular momentum with respect to the H channel, where the ratio $T(90°)/T(0°)$ is nearly unity (see Discussion section). The uncertainty in the $T(\theta)$ function is very small for the HCS channel: the $T(180°)/T(0°)$ ratio cannot be varied by more than ±0.08 and the $T(90°)/T(0°)$ ratio by not more than ±0.05 without worsening significantly the best-fit (i.e., putting the best-fit curve outside of the error bars).

For the HCS + CH_3 channel the $P(E'_T)$ in the forward 0°−60° angular range is more energetic than in the sideways (60°−140°) and backward (140°−180°) angular ranges. At the lower E_c (higher E_c) (a) in the range 0°−60° the $P(E'_T)$ peaks at about 29 (41) kJ mol^{-1}, with an average amount of energy in translation of 25 (33) kJ mol^{-1}, corresponding to 55% (58%) of the total available energy; (b) in the range 60°−140° the $P(E'_T)$ peaks at about 21 (31) kJ mol^{-1}, with an average amount of energy in translation of about 23 (30) kJ mol^{-1}, corresponding to 49% (52%) of the total available energy; (c) in the range 140°−180° the $P(E'_T)$ peaks at about 13 (17) kJ mol^{-1}, with an average amount of energy in translation of about 19 (24) kJ mol^{-1}, corresponding to 41% (42%) of the total available energy. The trends with angular ranges remain the same at the two E_cs, with the fraction of energy in translation increasing slightly with increasing E_c.

For the CH_2CHS + H channel the $P(E'_T)$ at the lower E_c (higher E_c) peaks at 8.7 (10.2) kJ mol^{-1}, with an average amount of energy in translation of 16.1 (18.9) kJ mol^{-1}, corresponding to 25.5% (25.5%) of the total available energy. In contrast, for the strongly exoergic $CH_2CS + H_2$ channel the $P(E'_T)$ is much more energetic, peaking at low (high) E_c at 122 (126) kJ mol^{-1}, with an average amount of energy in translation of about 128 (133) kJ mol^{-1}, corresponding to about 46% (46%) of the total available energy.

Ratio of Cross Sections for the Observed Channels. From the apparent cross sections (w_i weights in eq 7) obtained from

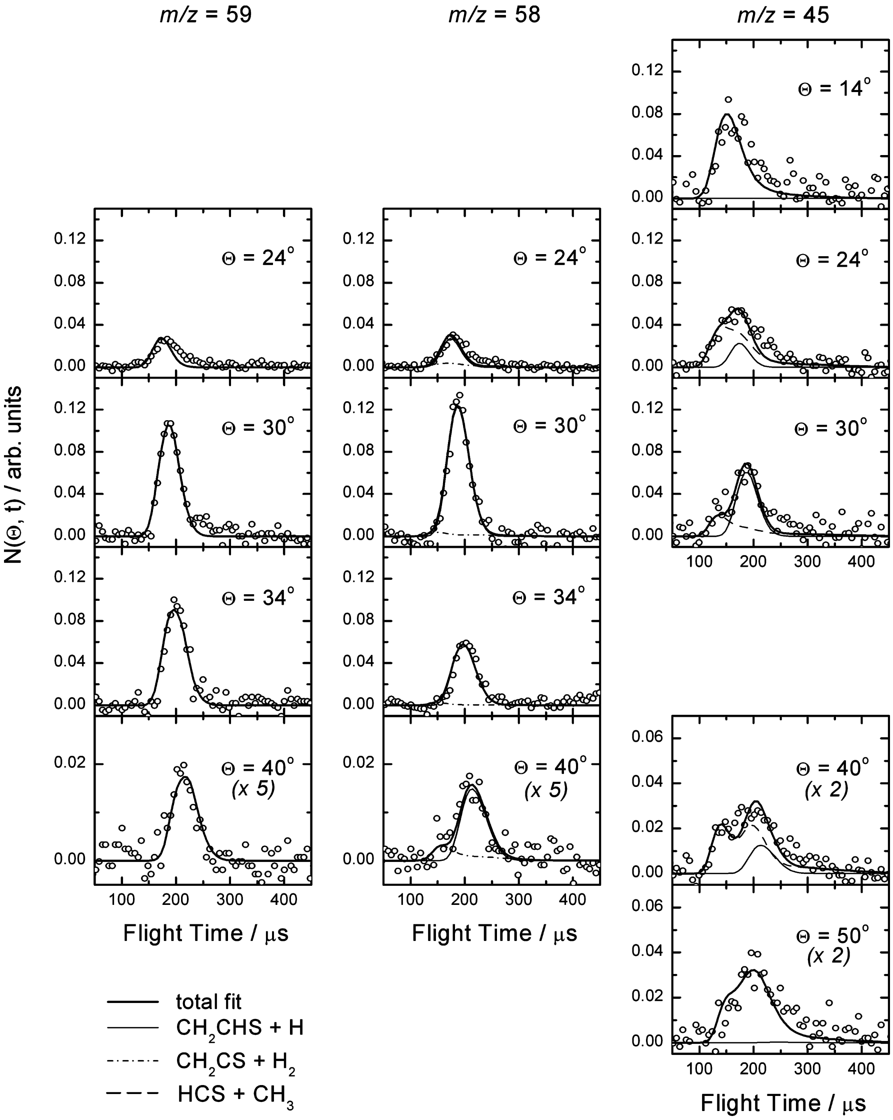

Figure 6. Time-of-flight distributions at the indicated LAB angles of the products at $m/z = 59$ (left panels), $m/z = 58$ (central panels), and $m/z = 45$ (right panels) for $E_c = 45.0$ kJ mol^{-1}. For $m/z = 59$ and 58 the TOF spectrum at $\Theta = 40°$ is amplified by a factor 5 for clarity. For $m/z = 45$ the TOF spectra at $\Theta = 40°$ and 50° are amplified by a factor 2 also for clarity. The various lines (symbols as in the legend) are the calculated distributions from the indicated contributing channels using the best-fit CM functions.

the best-fit procedure, taking into account the estimated product ionization cross sections, the measured quadrupole transmission at the different masses, and the estimated fragmentation patterns of the CH_2CHS, CH_2CS, and HCS products, the ratio of cross sections for the channels (1) (H channel), (3) (H_2 channel), and (4) (HCS channel) $\sigma_H:\sigma_{H_2}:\sigma_{HCS}$ are estimated to be 1.0:0.37:3.1 at $E_c = 37.0$ kJ mol^{-1} and 1.0:0.34:4.5 at $E_c = 45.0$ kJ mol^{-1}, with an uncertainty of about ±25%. The values reported here represent an improvement with respect to the preliminary estimate given in the previous Communication.[26] We have to add that the derived σ_{H_2}/σ_H ratio may actually be underestimated because thioketene (CH_2CS) may fragment significantly (by analogy with ketene) to CH_2^+, and we have not been able to separate this contribution at $m/z = 14$.

As far as the possible occurrence of other channels is concerned, we could not discriminate the HS product (channel (5)) from ^{33}S isotopic interferences, although we had indication of some reactive signal, while we did not have evidence of the occurrence of the endothermic channel (2) leading to $CH_3CS + H$. The detection of either product (CH_4 and CS) from the strongly exoergic channel (6) is very challenging under our experimental conditions and was not attempted, but we expect this channel to be minor because of the very high exit potential barrier of about 350 kJ mol^{-1} from the thioacetaldehyde intermediate (see Figure 10 in the next section). This expectation was corroborated by RRKM calculations (see section 4.4). The experimentally estimated ratios of cross sections will be compared with the results of RRKM calculations in the Discussion section.

4.3. Computational Results. *$S(^1D) + C_2H_4$.* The potential energy surface of $S(^1D) + C_2H_4$ has been investigated at the ab initio level. The lowest stationary points localized on this surface have been reported in Figure 9, where the main geometrical parameters (angstroms and degrees) are shown together with the energies computed at B3LYP/aug-cc-pV(T+*d*)Z and CCSD(T)/ aug-cc-pV(T+*d*)Z level, relative to that of thioacetaldehyde (CH_3CHS, **4s**) which is the most stable isomer at all levels of calculation. The energy changes and barrier heights computed at 0 K with inclusion of the zero point energy correction for the main isomerization and dissociation processes are reported in Table 2, while a schematic representation of the potential energy surface of the system $S(^1D) + C_2H_4$ is shown in Figure

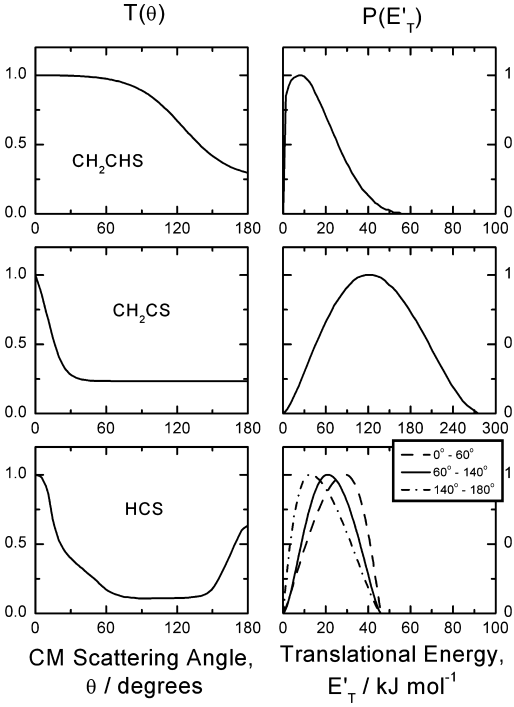

Figure 7. Best-fit CM product (left-hand side) angular and (right-hand side) translational energy distributions at $E_c = 37.0$ kJ mol^{-1} for the reaction channel $CH_2CHS + H$ (top panels), $CH_2CS + H_2$ (middle panels), and $HCS + CH_3$ (bottom panels). The angular dependence of the translational energy distribution for the $HCS + CH_3$ channel is indicated with different line symbols, as in the legend for the indicated angular ranges.

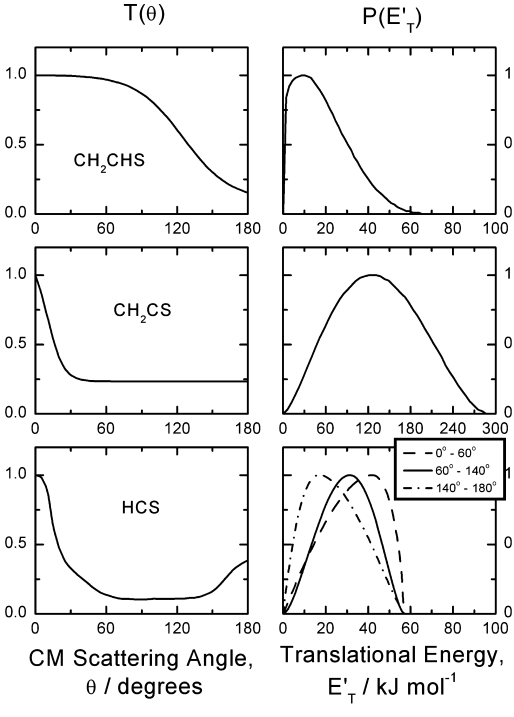

Figure 8. As in Figure 7, but for $E_c = 45.0$ kJ mol^{-1}.

10. For the sake of simplicity in Figure 10 we have reported only the relative energies computed at the CCSD(T)/aug-cc-pV(T+*d*)Z level with the W1 results in parentheses for selected processes, while in Table 2 we have reported the values computed at all levels of calculation for comparison purposes.

Many of the stationary points which are of interest in this work have been previously studied at both the semiempirical[54] and ab initio level.[55] The agreement of our work to those results is reasonable, the differences being due to the larger basis set and the different methods used in this work. In the following paragraph we will discuss our results; for simplicity we will refer only to the most accurate results, i.e., the CCSD(T) results. The reaction of S(^{1}D) with C_2H_4 can give rise to thiirane ($H_2C(S)CH_2$, **1s**) through the interaction of S with the C−C π bond or to ethenethiol (CH_2CHSH, **3s** or **3s′**) through the insertion of S into the C−H σ bond. Both these processes are barrierless, and the product formed depends on the initial orientation of S with respect to C_2H_4. The first process (addition) is the preferred one for most orientations and should be favored by the long-range interaction of the approaching reaction partners. Thiirane (**1s**) is more stable than the reactants by 347.1 kJ mol^{-1} at the CCSD(T) level and becomes even more stable at the W1 level (360.5 kJ mol^{-1}). However, from the W1 values reported in Figure 10 we can notice that the energy differences between CCSD(T) and W1 values are almost constant, suggesting that the difference between the two methods is mainly in the reactants. Thiirane (**1s**) can isomerize to *trans*-ethenethiol (**3s**), which is less stable by only 0.3 kJ mol^{-1}, with a barrier of 242.9 kJ mol^{-1} at CCSD(T) level (249.3 kJ mol^{-1} at W1 level). Alternatively, thiirane can dissociate to CH_2CS and H_2 with a higher barrier of 303.7 kJ mol^{-1} (304.1 kJ mol^{-1} at W1 level). *trans*-Ethenethiol (**3s**) can easily isomerize to *cis*-ethenethiol (**3s′**) with a barrier of only 8.0 kJ mol^{-1} (not shown in Figure 10 for simplicity). *trans*-Ethenethiol (**3s**) can isomerize to thioacetaldehyde (**4s**) with a barrier of 225.8 kJ mol^{-1} or to *trans*-ethylidenethiol (**5s**) with a higher barrier of 263.9 kJ mol^{-1}. *trans*-Ethenethiol (**3s**) can also dissociate in endothermic, barrierless reactions giving rise to the products $CH_2CHS + H$ or $C_2H_3 + HS$. The first reaction is endothermic by 331.7 kJ mol^{-1} and the second one by 347.4 kJ mol^{-1} from the intermediate complex. A similar pattern applies for the cis isomer. *cis*-Ethenethiol (**3s′**) can isomerize to thioacetaldehyde (**4s**) with a barrier of 232.6 kJ mol^{-1} or to *cis*-ethylidenethiol (**5s′**) with a higher barrier of 265.1 kJ mol^{-1}. *cis*-Ethenethiol (**3s′**) can also dissociate in endothermic, barrierless reactions giving rise to the products $CH_2CHS + H$ or $C_2H_3 + HS$. The first reaction is endothermic by 332.0 kJ mol^{-1} and the second one by 347.7 kJ mol^{-1} (again from the intermediate complex). Thioacetaldehyde (**4s**) can isomerize to *trans*-ethylidenethiol (**5s**) with a barrier of 307.0 kJ mol^{-1} or can dissociate to the products $CH_4 + CS$ with a slight higher barrier of 341.0 kJ mol^{-1}. Thioacetaldehyde can also isomerize to *trans*-CH_3SCH (**6s**), but this reaction shows a very high barrier of 390.2 kJ mol^{-1}. *trans*-Ethylidenethiol (**5s**) can isomerize to *cis*-ethylidenethiol (**5s′**) with a barrier of 120.7 kJ mol^{-1}. This relatively high barrier is due to the fact that a rotation around a C−S partial double bond is necessary. Ethylidenethiol can dissociate to the products $CH_3CS + H$ in an endothermic, barrierless process. Also *trans*-CH_3SCH (**6s**) can isomerize to the corresponding cis isomer (**6s′**); this reaction shows a barrier of 87.7 kJ mol^{-1} due to the rotation around the S−C partial double bond. CH_3SCH can dissociate to the products $CH_3 + HCS$ in a barrierless reaction which is endothermic by 160.5 kJ mol^{-1} for the trans isomer and 150.7 kJ mol^{-1} for the cis one, but exoergic for the reactants.

S(^{3}P) + C_2H_4. The potential energy surface of S(^{3}P) + C_2H_4 has been investigated at ab initio level. The lowest stationary points localized on this surface are reported in Figure 11, where the main geometrical parameters (angstroms and degrees) are shown together with the energies computed at the B3LYP/aug-

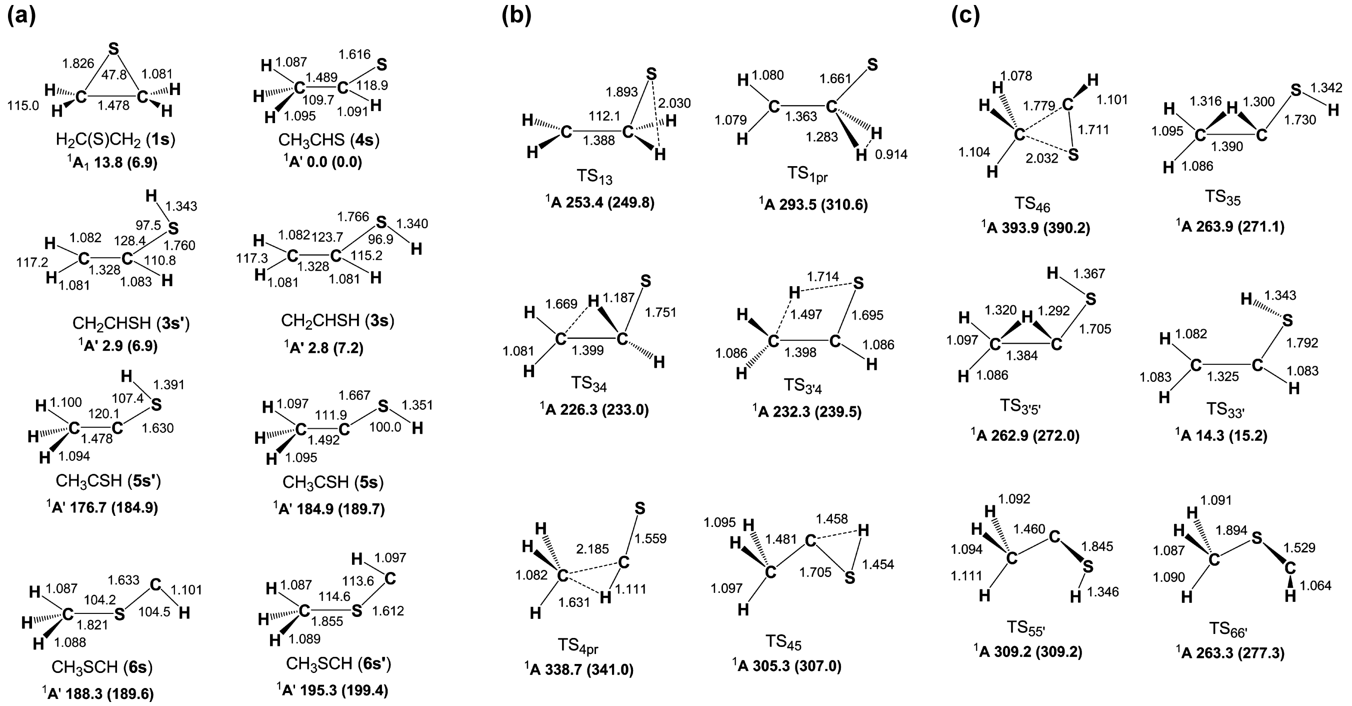

Figure 9. B3LYP optimized geometries (angstroms and degrees) and relative energies (kJ mol^{-1}) at 0 K of minima (a) and saddle points (b and c) localized on the PES of S(^{1}D) + C_2H_4; CCSD(T) relative energies are reported in parentheses.

TABLE 2: Enthalpy Changes and Barrier Heights (kJ mol^{-1}, 0 K) Computed at the B3LYP/aug-cc-pV(T+*d*)Z, CCSD(T)/aug-cc-pV(T+*d*)Z, and W1 Levels of Theory for Selected Dissociation and Isomerization Processes for the System S(^{1}D) + C_2H_4

	$\Delta H_0°$			barrier height		
	B3LYP	CCSD(T)	W1	B3LYP	CCSD(T)	W1
$H_2C(S)CH_2 \rightarrow S(^1D) + C_2H_4$	335.2	347.1	360.5			
$H_2C(S)CH_2 \rightarrow H_2C(S)CH + H$	406.7	417.2				
$H_2C(S)CH_2 \rightarrow CH_2CHSH$ (**3s**)	−11.0	0.3		239.6	242.9	249.3
$CH_3CHS \rightarrow CH_2CHSH$ (**3s**)	2.8	7.2		226.3	233.0	233.5
$CH_3CHS \rightarrow CH_2CHSH$ (**3s′**)	2.9	6.9		233.2	239.5	
$CH_3CHS \rightarrow CH_3CSH$ (**5s**)	184.9	188.5		305.3	307.0	
CH_2CHSH (**3s**) $\rightarrow CH_3CSH$ (**5s**)	182.1	182.5		261.1	263.9	
CH_2CHSH (**3s′**) $\rightarrow CH_3CSH$ (**5s′**)	173.8	178.0		260.0	265.1	
CH_2CHSH (**3s**) $\rightarrow CH_2CH + HS$	329.3	347.3				
CH_2CHSH (**3s**) $\rightarrow CH_2CHSH$ (**3s′**)	0.1	−0.3		11.5	8.0	
CH_2CHSH (**3s**) $\rightarrow CH_2CHS + H$	321.6	331.7				
CH_2CHSH (**3s**) $\rightarrow CH_2CSH + H$	418.7	430.4				
CH_3CSH (**5s**) $\rightarrow CH_3CSH$ (**5s′**)	−8.2	−4.8		124.3	120.7	
CH_3SCH (**6s**) $\rightarrow CH_3SCH$ (**6s′**)	7.0	9.8		75.0	87.7	
$CH_3CHS \rightarrow CH_3SCH$ (**6s**)	188.3	189.6		393.9	390.2	
$CH_3CHS \rightarrow CS + CH_4$	130.7	126.2	131.9	338.7	341.0	
$H_2C(S)CH_2 \rightarrow CH_2CS + H_2$	87.9	115.4	115.9	279.7	303.7	304.1
$CH_3CHS \rightarrow CH_3CS + H$	364.9	376.9	378.0			
$CH_3CHS \rightarrow CH_3 + HCS$	328.3	350.1	356.5			
CH_3CSH (**5s**) $\rightarrow CH_3CS + H$	180.0	187.2				
CH_3SCH (**6s**) $\rightarrow CH_3SC + H$	357.8	360.5				
CH_3CSH (**5s′**) $\rightarrow CH_3CS + H$	188.2	192.0				
CH_3CSH (**5s**) $\rightarrow CH_3 + HSC$	304.5	319.1				
CH_3SCH (**6s**) $\rightarrow CH_3 + HCS$	140.0	160.5				
CH_3CSH (**5s′**) $\rightarrow CH_3 + HSC$	312.7	323.9				
$CH_3CS \rightarrow CH_2CHS$	−40.5	−38.0	−38.6	146.5	158.4	

cc-pV(T+*d*)Z and CCSD(T)/ aug-cc-pV(T+*d*)Z levels, relative to that of species CH_3CHS (**4t**) which is the most stable isomer on the triplet surface at all levels of calculation. The energy changes and barrier heights computed at 0 K with inclusion of the zero point energy correction for the main isomerization and dissociation processes are reported in Table 3, while a schematic representation of the potential energy surface of the system S(^{3}P) + C_2H_4 is shown in Figure 12. For the sake of simplicity in Figure 12 we have reported only the relative energies computed at the CCSD(T)/aug-cc-pV(T+*d*)Z level with the W1 results in parentheses for selected processes, while in Table 3 we have reported the values computed at all levels of calculation for comparison purposes. In order to allow a comparison with the singlet surface, in Figure 12 we use the same zero level energy used in Figure 10. Some of the stationary points which are of interest in this work have been previously studied at the ab initio

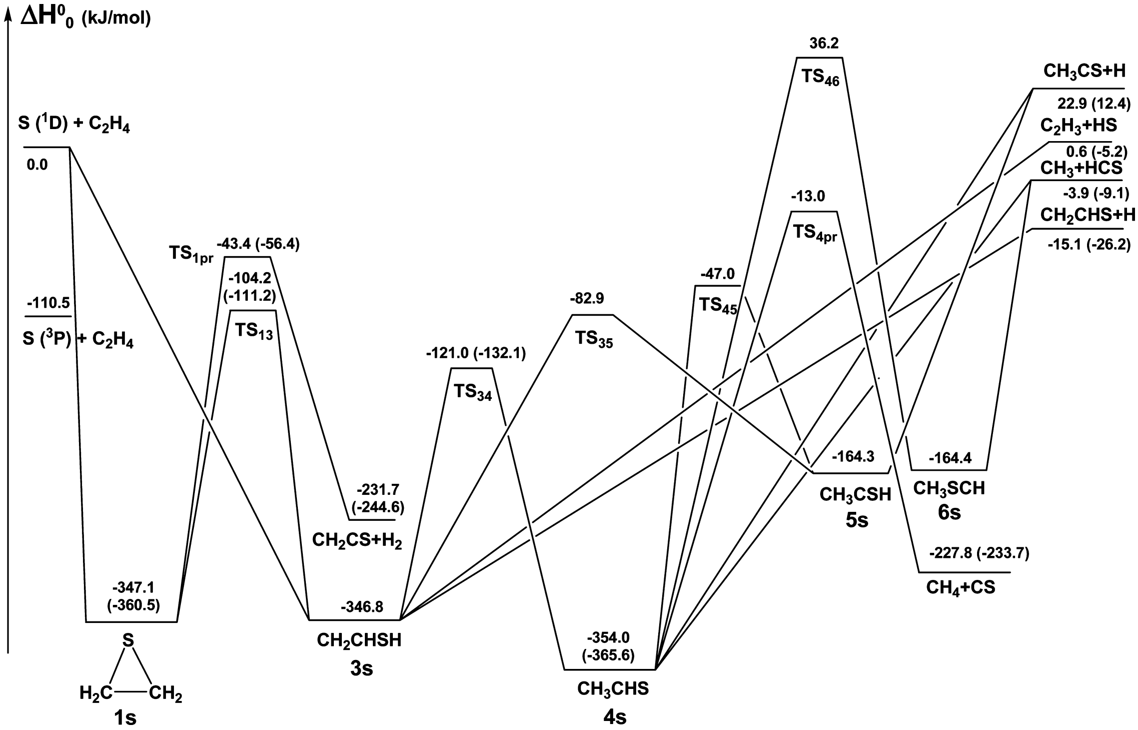

Figure 10. Schematic representation of the S(^{1}D) + C_2H_4 potential energy surface. For simplicity, only the CCSD(T) relative energies (kJ mol^{-1}) are reported. For selected reactions W1 relative energies (kJ mol^{-1}) are reported in parentheses. The minima **3s′**, **5s′**, and **6s′** are omitted for clarity.

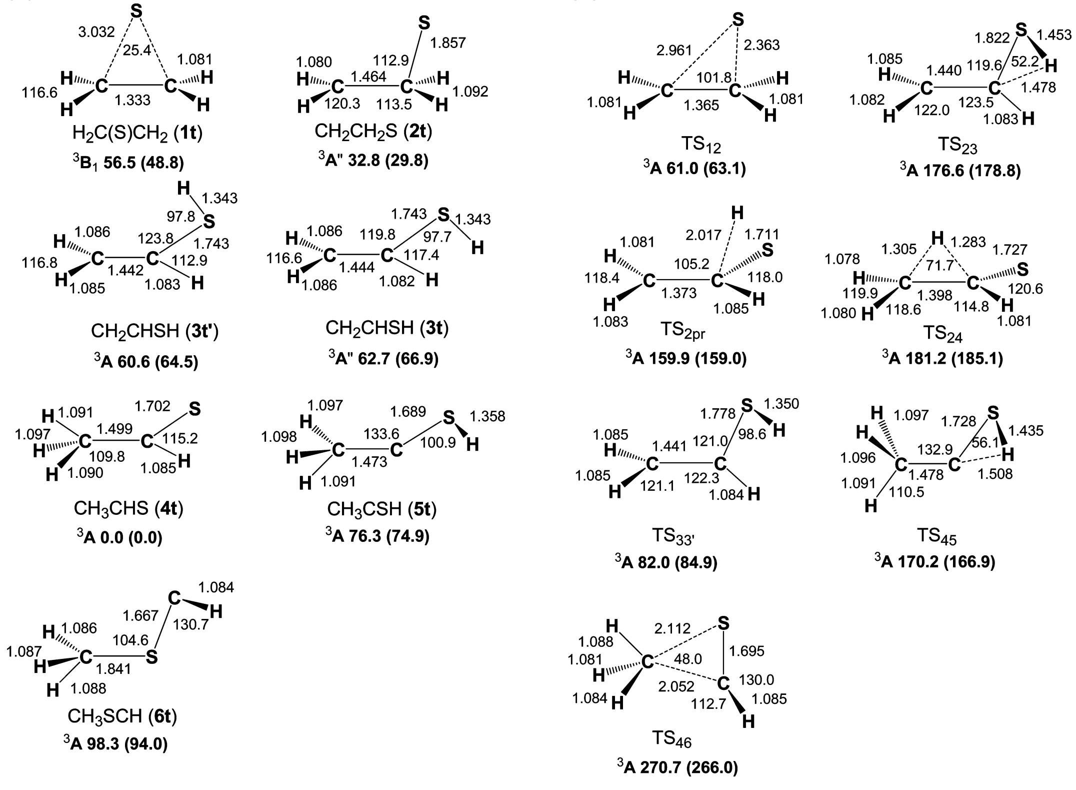

Figure 11. B3LYP optimized geometries (angstroms and degrees) and relative energies (kJ mol^{-1}) at 0 K of minima (a) and saddle points (b) localized on the PES of S(^{3}P) + C_2H_4; CCSD(T) relative energies are reported in parentheses.

level.[55a,56] The agreement of our work to those results is reasonable, the differences being due to the larger basis set and the different methods used in this work. In particular we can compare the energy for the reaction S(^{3}P) + C_2H_4 → CH_2CHS + H, reported in Table 3, with that recently computed by Woon using very accurate methods.[56] Our values are in very good agreement with the values computed by Woon at a comparable level of calculation: 95.4 kJ mol^{-1} with respect to 96.1 kJ mol^{-1}

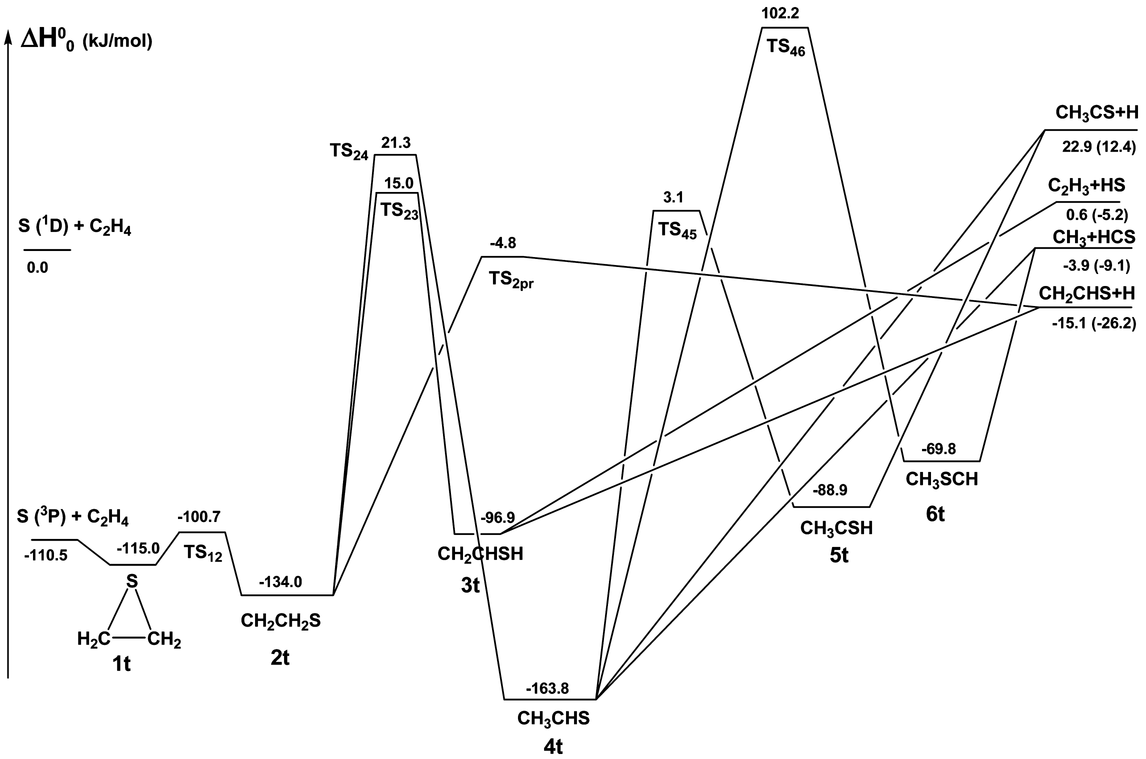

Figure 12. Schematic representation of the S(^{3}P) + C_2H_4 potential energy surface. For simplicity, only the CCSD(T) relative energies (kJ/mol) are reported. For selected reactions W1 relative energies (kJ mol^{-1}) are reported in parentheses. The minimum **3t′** is omitted for clarity.

TABLE 3: Enthalpy Changes and Barrier Heights (kJ mol^{-1}, 0 K) Computed at the B3LYP/aug-cc-pV(T+*d*)Z, CCSD(T)/aug-cc-pV(T+*d*)Z and W1 Levels of Theory for S(^{3}P) + C_2H_4

	$\Delta H_0°$			barrier height	
	B3LYP	CCSD(T)	W1	B3LYP	CCSD(T)
$H_2C(S)CH_2 \rightarrow S(^3P) + C_2H_4$	6.6	4.5			
$S(^3P) + C_2H_4 \rightarrow CH_2CHS + H$	85.9	95.4	84.3		
$H_2C(S)CH_2 \rightarrow CH_2CH_2S$	−23.7	−19.0		4.5	14.3
$CH_2CH_2S \rightarrow CH_2CHSH$ (**3t**)	29.9	37.1		143.8	149.0
$CH_2CH_2S \rightarrow CH_3CHS$	−32.8	−29.8		148.4	155.3
$CH_2CH_2S \rightarrow CH_2CHS + H$	116.2	118.9		127.1	129.2
$CH_3CHS \rightarrow CH_2CHSH$ (**3t**)	62.7	66.9			
$CH_3CHS \rightarrow CH_3CSH$	76.3	74.9		170.2	166.9
CH_2CHSH (**3t**) $\rightarrow CH_2CH + HS$	94.0	97.5			
CH_2CHSH (**3t′**) $\rightarrow CH_2CH + HS$	96.1	99.9			
CH_2CHSH (**3t**) $\rightarrow CH_2CHSH$ (**3t′**)	−2.1	−2.4		19.3	18.0
CH_2CHSH (**3t**) $\rightarrow CH_2CHS + H$	86.2	81.8			
CH_2CHSH (**3t′**) $\rightarrow CH_2CHS + H$	88.3	84.2			
$CH_3CHS \rightarrow CH_3SCH$	98.3	94.0		270.7	266.0
$CH_3CHS \rightarrow CH_3CS + H$	189.5	186.7			
$CH_3CHS \rightarrow CH_3 + HCS$	152.9	159.9			
$CH_3CSH \rightarrow CH_3CS + H$	113.1	111.8			
$CH_3CSH \rightarrow CH_3 + HSC$	237.7	243.8			
$CH_3SCH \rightarrow CH_3 + HCS$	54.6	65.9			
$CH_3SCH \rightarrow CH_3SC + H$	272.4	265.8			

which is the best estimate of Woon. Our best estimate, however, is slight lower being the value 84.3 kJ mol^{-1} computed at the W1 level.

In this paragraph we will present our results; for simplicity we will refer only to the most accurate results, i.e., the CCSD(T) results. The interaction of S(^{3}P) with C_2H_4 gives rise to species $H_2C(S)CH_2$ (**1t**), where the sulfur atom interacts very weakly with the C−C π bond: the distance between the sulfur atom and the midpoint of the C−C bonding is 2.958 Å and the binding energy is only 4.5 kJ mol^{-1}. Species **1t** can easily isomerize to species CH_2CH_2S (**2t**) with a barrier of only 14.3 kJ mol^{-1}. **2t** can dissociate to the products CH_2CHS + H with a relatively high barrier of 129.2 kJ mol^{-1}. This part of the surface has been previously studied also by Woon,[56] and we agree with his results. However, **2t** can also isomerize to species *trans*-CH_2CHSH (**3t**) or to species CH_3CHS (**4t**) with barriers of 149.0 and 155.3 kJ mol^{-1}, respectively. *trans*-CH_2CHSH (**3t**) can easily isomerize to the corresponding cis isomer (**3t′**) with a barrier of only 18.0 kJ mol^{-1} or can dissociate to the products CH_2CHS + H or CH_2CH + HS in endothermic reactions. Species **4t** can dissociate to the products CH_3 + HCS or CH_3CS + H in endothermic, barrierless reactions or can isomerize to species CH_3CSH (**5t**) with a barrier of 166.9 kJ mol^{-1} or to species CH_3SCH (**6t**) with an even higher barrier of 266.0 kJ mol^{-1}.

TABLE 4: Microcanonical Rate Constants for Reaction Channels of the Indicated C_2H_4S Intermediates, in Units of s^{-1}, at the Two Experimental Collision Energies[a]

	$E_c = 37.0$ kJ mol^{-1}	$E_c = 45.0$ kJ mol^{-1}
$k_{1s\to 3s}$	6.161×10^{9}	8.016×10^{9}
$k_{1s\to CH_2CS+H_2}$	4.163×10^{8}	6.268×10^{8}
$k_{3s\to 1s}$	7.676×10^{7}	1.001×10^{8}
$k_{3s\to 4s}$	3.303×10^{8}	4.076×10^{8}
$k_{3s\to 5s}$	4.724×10^{7}	6.356×10^{7}
$k_{3s\to CH_2CHS+H}$	8.437×10^{6}	1.634×10^{7}
$k_{3s\to CH_2CH+HS}$	1.743×10^{8}	2.634×10^{8}
$k_{4s\to 3s}$	3.028×10^{9}	3.753×10^{9}
$k_{4s\to 5s}$	1.031×10^{8}	1.588×10^{8}
$k_{4s\to CH_4+CS}$	6.646×10^{6}	1.305×10^{7}
$k_{4s\to CH_3+HCS}$	3.252×10^{8}	6.881×10^{8}
$k_{4s\to CH_3CS+H}$	1.350×10^{4}	5.409×10^{4}
$k_{5s\to 3s}$	9.598×10^{10}	1.117×10^{11}
$k_{5s\to 4s}$	2.260×10^{10}	3.004×10^{10}
$k_{5s\to CH_3CS+H}$	5.612×10^{7}	1.333×10^{8}

[a] See text for details.

TABLE 5: Total Branching Ratios for Dissociation Channels at the Two Experimental Collision Energies[a]

	$E_c = 37.0$ kJ mol^{-1}	$E_c = 45.0$ kJ mol^{-1}
$CH_2CS + H_2$	0.084, 0.022	0.092, 0.021
$CH_2CHS + H$	0.036, 0.038	0.043, 0.047
$CH_2CH + HS$	0.741, 0.791	0.695, 0.749
$CH_4 + CS$	0.003, 0.003	0.003, 0.003
$CH_3 + HCS$	0.136, 0.145	0.167, 0.180
$CH_3CS + H$	0.0001,0.0001	0.0002,0.0002

[a] The two ratios pertain to addition and insertion, respectively, as the initial reaction step (see text for details).

The dissociations of species **5t** to the products $CH_3CS + H$ and species **6t** to the products $CH_3 + HCS$ are both barrierless reactions but strongly endoergic for $S(^3P)$.

4.4. RRKM Results. Using our RRKM algorithm, we have calculated first-order microcanonical rate constants for all rearrangements between intermediates and all dissociation steps. As previously mentioned, for all dissociation steps without a barrier, the calculation has been performed in a variational manner. At various points along the dissociation coordinate, the local potential energy, vibrational frequencies, and rotational constants (excluding the dissociation coordinate itself) were obtained and the dissociation rate constant was calculated. The intermediate point resulting in the minimum rate constant was taken as the transition state of the dissociation.

At the end of the calculation we have a matrix of rate constants and branching ratios, from each intermediate to each intermediate or dissociation channel. The branching ratio matrix is stochastic, and in order to convert these branching ratios into the total ones pertaining to the dissociation channels, we have evaluated the limit of multiplying this matrix with itself up to infinity. The limiting matrix is the one containing the total branching ratios.

In Table 4 are shown the absolute rate constants for each unimolecular step of the reaction, and in Table 5 two relevant branching ratios are shown. As mentioned before, it is not clear what fraction of the initial reaction events proceed by addition (leading to thiirane, denoted as intermediate **1s**) or by insertion (leading to CH_2CHSH, denoted as intermediate **3s**). We have determined total branching ratios for the two extreme cases (100% addition or 100% insertion) and the two branching ratios refer respectively to these two extremes.

In both cases, and for both collision energies, the dissociation channel $CH_2CH + HS$ is by far the most abundant one (its branching ratio ranging between 0.7 and 0.8). This is the result of a combination of many low-frequency vibrational modes and a low energy of the transition state with respect to other dissociation channels. A particularly striking manifestation of the predominance of this channel is the fact that, even though it is a product of the dissociation of CH_2CHSH and, therefore, would be expected to be much more abundant if the initial step is insertion as opposed to addition, it is seen that its branching ratio drops only marginally from one case to another (from 0.791 to 0.741 at the lower and from 0.749 at 0.695 at the higher energy).

The second most abundant channel (again for both cases and both collision energies) is the one leading to $CH_3 + HCS$. Its branching ratio at a collision energy of 37 kJ mol^{-1} is around 0.14−0.15, increasing to 0.17−0.18 at 45 kJ mol^{-1}. At both energies, the branching ratio increases if insertion is considered to be the initial step but not considerably, since this channel proceeds from the dissociation of CH_3CSH. According to the reaction scheme in Figure 10, insertion (as opposed to addition) reduces the number of rearrangement steps necessary from 2 to 1 and thus is not expected to favor this channel by a large factor.

The channel significantly affected by the initial choice of addition/insertion is the dissociation of thiirane into $CH_2CS + H_2$. It is obvious that this should be the case, since this dissociation can only take place from thiirane and an initial formation of it through addition should increase its branching ratio considerably. On the other hand, if the initial step is insertion (and consequent formation of CH_2CHSH), then an additional rearrangement step into thiirane is required. This requirement heavily penalizes formation of H_2. In fact, it is seen that, with addition as an initial step, the branching ratio at 37 kJ mol^{-1} is 0.084, increasing to 0.092 at 45 kJ mol^{-1}. In the insertion case, the corresponding values are 0.022 and 0.021, around four times lower.

The channel leading to $CH_2CHS + H$ is dominated by $CH_2CS + H_2$ in the addition case, its branching ratios being 0.036 and 0.043 at the two collision energies (see Table 5). The pattern is inverted in the insertion case. The branching ratios of $CH_2CHS + H$ remain almost constant (branching ratios 0.038 and 0.047, respectively, see Table 5), while, as previously seen, those for $CH_2CS + H_2$ drop drastically. Even though $CH_2CHS + H$ is a product of the dissociation of CH_2CHSH (the insertion adduct), its branching ratio increases only marginally through the addition/insertion spectrum due to its low absolute rate constant (of the order of 10^7 s^{-1}). The ratio between the two channels $(CH_2CHS + H)/(CH_2CS + H_2)$ ranges from around 0.5 in the addition case up to 2 in the insertion one. As the most likely initial step appears to be addition, the RRKM prediction appears to be one of predominance of the H_2 channel over the H one. On the other hand, as regards the ratio between the channels $(CH_3 + HCS)/(CH_2CHS + H)$, this appears to be relatively constant at a value range 3.8−3.9, with respect both to the collision energy and to the choice of addition or insertion as the initial step. Again, this is to be expected since the extra step of rearrangement from thiirane to CH_2CHSH has to be taken by all dissociation channels (with the exception of $CH_2CS + H_2$).

Minor channels include the dissociation of CH_3CHS into $CH_4 + CS$ and the endothermic dissociation into $CH_3CS + H$. The branching ratio of the former channel stays in the region of 0.003, marginally increasing with collision energy and insertion as opposed to addition (in line with the observations made so far). The latter channel can result both from the direct dissociation of CH_3CHS and from rearrangement from CH_3CHS to CH_3CSH and dissociation of the latter species. Nevertheless, the highly endothermic nature of the channel leads to very low absolute rate constants (of the order of 10^4 s^{-1}) and branching ratios (around 0.0001−0.0002).

Generally, the intermediate CH_3CSH (denoted **5s**) contributes to the overall scheme only by offering an alternative dissociation pathway to the $CH_3CS + H$ channel. Even though the absolute rate constant for this dissociation is around 3 orders of magnitude higher than the rate constant from CH_3CHS to the same channel, it nevertheless has a very minor probability of occurring, rearrangement into CH_2CHSH and CH_3CHSH being vastly preferred (with an absolute rate constant of the order of 10^{11} s^{-1}).

In order to assess the effect of the transition states for dissociation, we have compared the rate constants and branching ratios presented here with the ones derived assuming that the transition state lies far in the product valley. It is clear that all dissociation rate constants derived using this hypothesis will be larger than the ones presented using the variational principle. The most dramatic effect is the increase of the rate constants of the channels $CH_2CHS + H$ and $CH_3 + HCS$ by 1−2 orders of magnitude and the consequent increase of their branching ratios. The branching ratio of the former channel reaches values of 0.33−0.35 while for the latter one the increase is much less spectacular (0.23 at the lower energy and 0.18 at the higher energy) due to the extra rearrangement step required. By comparison, the absolute rate constant for the $CH_2CH + HS$ channel increases only by a factor of about 4, causing a drastic drop in its branching ratio which reaches values of about 0.37−0.38, comparable to those for $CH_2CHS + H$. Obviously, since the rate constant for $CH_2CS + H_2$ does not change (being a "tight" transition state), its branching ratio drops to values around 0.07 for both energies and it is now heavily dominated by all three main dissociation channels.

5. Discussion

In the following discussion we refer to Figure 10 which shows the energy level and correlation diagram of the singlet C_2H_4S PES as from the present electronic structure calculations. In the light of the experimental and theoretical results presented in section 4, we can state that the $S(^1D) + C_2H_4$ reaction occurs readily without any entrance potential barrier. In fact, the kinetics measurements show a rate coefficient for removal of $S(^1D)$ by C_2H_4 which is very fast (close to the gas-kinetic collisional limit) and show very little dependence on temperature. While it was not possible to distinguish between reaction and quenching in these kinetic measurements, the lack of any significant temperature dependence of the overall rate coefficient points strongly to the absence of any real barrier on the reactive PES, and indeed an entrance barrier has not been found theoretically. Measurements currently in progress on the pure collisional deactivation or quenching of $S(^1D)$ by N_2 and Ar show rate coefficients around 3−5 and 30−35 times slower than that for C_2H_4, respectively, apparently with very little temperature dependence.[33] If the collisional quenching part of the total $S(^1D) + C_2H_4$ removal rate coefficient displays similar behavior, then we can conclude that the reactive rate coefficient indeed shows very little temperature dependence: otherwise, we would have expected to see at least some significant decrease in the overall rate coefficient at low temperatures.

One important question to address is whether the chemical reaction accounts fully for the total $S(^1D)$ loss, or only for a fraction of it. Black[28] measured the branching ratio for quenching and reaction in the interaction of $S(^1D)$ and C_2H_4 in his kinetic studies, using 248 nm photodissociation of OCS to generate $S(^1D)$, and monitoring $S(^3P)$ by resonance-enhanced photoionisation at 311 nm. The branching ratios obtained at 300 K, 0.77 ± 0.05 for quenching and 0.23 ± 0.05 for reaction, were based on the assumption that only a negligible concentration of $S(^3P)$ atoms was produced by the photolysis of OCS, and a correction had to be considered as $S(^3P)$ reacts slowly with C_2H_4 ($k(300\ K) = (5.1 \pm 0.5) \times 10^{-13}$ cm^3 $molecule^{-1}$ s^{-1}). Although the reactive fraction is smaller than a previous estimate by Gunning and co-workers[57] (quoted in ref 28) who found an upper limit of 0.52 for quenching, and a minimum value of 0.48 for reaction, overall the early kinetics studies point to a large fraction of physical quenching in the $S(^1D) + C_2H_4$ interaction. In any case, it is not possible to extrapolate these room temperature results to lower temperatures. Unfortunately, our kinetics work does not provide information on this issue, and neither do the present CMB experiments. There is clearly a need for direct kinetics experiments to investigate this branching ratio as a function of temperature and/or collision energy. In principle, the CMB technique should be able to provide some information by exploiting TOF energy loss measurements, but because of the very large background at $m/z = 32$ due to elastically scattered S-atoms, and a large concentration of $S(^3P)$ in the beam, we were not able to observe any fast S atoms coming from electronic to translational energy transfer in $S(^1D) + C_2H_4$ collisions leading to $S(^3P) + C_2H_4$. The singlet intermediates are lower in energy than the triplet intermediates (see Figures 10 and 12), and therefore the singlet and triplet PESs cross each other. Unfortunately, our calculations do not provide information on the nonadiabatic coupling terms.

According to our experimental results, we have no evidence of any dynamic signature, within our sensitivity, that the system crosses from the singlet to the triplet PES on its way to the observed products. We note, however, that if ISC takes place in the regions of the CH_2CHSH or CH_3CHS structures it would be difficult to disentangle a ISC contribution because of the expected similar reaction mechanism. On the other hand, a contribution to the observed channels from the $S(^3P)$ reaction via ISC from the triplet to the singlet PES is unlikely. As a matter of fact, even though Davis et al.[58] found a room temperature value of 5.0×10^{-13} cm^3 $molecule^{-1}$ s^{-1} and a small activation barrier of 6.6 kJ mol^{-1} for the $S(^3P) + C_2H_4$ reaction, all the possible ^3P reaction channels are endothermic with the exception of the channels leading to $CH_2CS(X^1A_1) + H_2(X^1\Sigma_g)$ and $CS(X^1\Sigma^+) + CH_4(X^1A_1)$ which would become accessible *only* if ISC from the triplet to the singlet PES occurs to a significant extent. However, our data do not support the occurrence of ISC for the former channel; in fact, the $P(E'_T)$ distribution for the H_2 elimination channel at low E_c (see middle panel on the right-hand side of Figure 7) extends up to about 275 kJ mol^{-1}, consistently with the total available energy of the $S(^1D)$ reaction (the total available energy is given by ($E_c - \Delta H_0°$) = (37.0 + 244.6) = 281.6 kJ mol^{-1}. Clearly, further experimental and theoretical investigation is needed to explore the role of physical quenching in $S(^1D) + C_2H_4$ interactions and in general of ISC in $S(^3P, ^1D) + C_2H_4$ collisions.

We will now discuss the reaction mechanism derived from our experimental and theoretical results. The CM angular and translational energy distributions for the three observed channels shown in Figures 7 and 8 allow an evaluation of the dynamical influence of the PES and of kinematic constraints. In particular, the $T(\theta)$ functions contain detailed information on the reaction mechanism and the $P(E'_T)$ functions on the product energy partitioning.

5.1. Angular Distributions. The best-fit CM angular distributions derived for the CH_2CHS, CH_2CS, and HCS products (Figures 7 and 8, left-hand side) show intensity in the whole angular range, but they are not backward−forward symmetric, as one would expect if the reaction proceeded through a long-lived complex, i.e., a complex with a lifetime of several rotational periods.[53] The best-fit $T(\theta)$ for all three observed reaction channels exhibits more intensity in the forward direction than in the backward direction, with the degree of asymmetry slightly increasing with increasing E_c. In general the shape of $T(\theta)$, that is its relative peaking at the poles ($\theta = 0°$ and $180°$) with respect to $\theta = 90°$, is dictated by the angular momentum disposal or the degree of correlation between reactant and product angular momenta[53] and provides information about the disposal of the total angular momentum into product rotation. For a generic bimolecular reaction, the conservation of total angular momentum $\boldsymbol{J}$ dictates: $\boldsymbol{J} = \boldsymbol{J}'$, where $\boldsymbol{J} = \boldsymbol{L} + \boldsymbol{j}$ and $\boldsymbol{J}' = \boldsymbol{L}' + \boldsymbol{j}'$, with $\boldsymbol{L}(\boldsymbol{L}')$ and $\boldsymbol{j}(\boldsymbol{j}')$ being the reactant (product) orbital and rotational angular momentum, respectively. Usually in crossed-beam experiments, because of the strong rotational cooling occurring in supersonic beams, $\boldsymbol{j}$ is small and can be assumed ≈ 0. For a complex-forming reaction, such as the title reaction, $\boldsymbol{J}$ ($\approx \boldsymbol{L}$) is disposed into $\boldsymbol{L}'$ and $\boldsymbol{j}'$ of the molecular products. If the molecular product receives little rotational excitation, $\boldsymbol{j}'$ is small, then $\boldsymbol{L}' \approx \boldsymbol{L}$, and the product relative velocity vector is constrained to lie in the same plane as the reactant relative velocity vector, that is, we have a "coplanar" reaction ($\boldsymbol{L}$ and $\boldsymbol{L}'$ are parallel or antiparallel). In this case a backward−forward symmetric $T(\theta)$ arises with a sharp peaking at the poles.

The situation discussed above is that occurring for the CH_3 + HCS channel, as can be inferred from the HCS $T(\theta)$ depicted in Figures 7 and 8 (bottom left panels). There are two main aspects in the HCS $T(\theta)$ function: (i) It is backward−forward distributed with a marked forward bias, which indicates that the reaction is proceeding through the formation of an osculating complex. (ii) It is strongly polarized, which indicates that there is a strong $\boldsymbol{L}$-$\boldsymbol{L}'$ coupling and a very low rotational excitation of the products; the latter implies that dissociation is coplanar and that most of the product internal excitation is vibrational excitation of the CH_3 and HCS moieties. An estimate of the lifetime for the complex formed at the two E_cs can be obtained by means of $T(180°)/T(0°) = \exp(-\tau_r/2\tau)$, where τ is the lifetime of the decomposing complex, τ_r its rotational period, and $T(180°)$ and $T(0°)$ are the values assumed by the $T(\theta)$ function at the two poles. The $T(180°)/T(0°)$ ratios of 0.634 at low E_c and 0.385 at high E_c indicate $\tau/\tau_r = 1.1$ and 0.5, respectively.

The dynamics of the CH_2CHS + H channel differs significantly from that of the HCS + CH_3 channel, partly because of the mass combination. Because of the small reduced mass of the products for this channel, large rotational excitation of the CH_2CHS product is expected on the basis of angular momentum partitioning arguments. In fact, it should be noted that, if $\boldsymbol{j}'$ is sizable, then $\boldsymbol{L}' < \boldsymbol{L}$, and products can scatter out of the plane containing the initial relative velocity vector, yielding a much less polarized or even isotropic $T(\theta)$. This is indeed the case portrayed by the $T(\theta)$ for the H channel (see Figures 7 and 8, top left panels). The asymmetry reflects an osculating complex mechanism, while the flat intensity from 0° to 90° suggests that the $T(\theta)$ would be isotropic at very low E_c mirroring a high product rotational excitation.

The $T(\theta)$ for the CH_2CS + H_2 channel also reflects an osculating complex mechanism in which the mean complex lifetime is only a fraction of its rotational period (from the asymmetry ratio $T(180°)/T(0°) \sim 0.23$ we derive $\tau/\tau_r \sim 0.3$).

As Figure 10 shows, following the $S(^1D)$ addition to the double bond of ethene the thiirane intermediate (**1s**) is formed. Thiirane undergoes in part a rapid ring-opening and a three-center H_2 elimination via transition state $\mathbf{TS}_{1pr}$ (see Figure 9), while the rest can isomerize by ring-opening (via $\mathbf{TS}_{13}$) to CH_2CHSH (**3s**) which competitively can undergo S−H bond cleavage to H + CH_2CHS (thiovinoxy) (exoergic by 26.2 kJ mol^{-1} with respect to the reactant asymptote) or isomerization (via $\mathbf{TS}_{34}$) to more stable thioacetaldehyde CH_3CHS (**4s**) which in turn can undergo C−C bond fission to CH_3 + HCS (exoergic by 9.1 kJ mol^{-1}). Because of the high stability of the thioacetaldehyde intermediate, a considerable lifetime of this complex is expected, larger than that for **3s**. This trend in average complex lifetime (supported by the RRKM results, see Table 4) is in line with the trend in the backward/forward asymmetry of the $T(\theta)$ for the CH_2CHS + H channel. Because the barrier to **3s**−**4s** isomerization is much lower than the CH_2CHS + H asymptote, this process is very likely to occur; that is, we expect a larger cross section for CH_3 + HCS than for CH_2CHS + H. RRKM results support these expectations (see Table 5).

5.2. Product Energy Distributions. The average fraction of total available energy released as recoil energy, $\langle E'_T \rangle$, is quite different for the three observed channels. While $\langle E'_T \rangle$ for the H forming channel is nearly statistical (about 25% of the total energy), and reflects a barrierless S−H bond rupture from CH_2CHSH, for the H_2 elimination channel the $\langle E'_T \rangle$ corresponds to about 46% of the total available energy, and this reflects a large exit potential barrier. This is consistent with a mechanism that sees the decomposition of **1s** via a tight transition state located at the top of a high barrier, which as Figure 10 shows is about 300 kJ mol^{-1} above the **1s** minimum and about 190 kJ mol^{-1} above the product asymptote. During the ring-opening process (see transition state geometry $\mathbf{TS}_{1pr}$ in Figure 9) and three-center H_2 elimination, a very large fraction of the potential energy of the exit barrier is channeled into recoil energy of the CH_2CS and H_2 cofragments (the $P(E'_T)$ peaks at about 120 kJ mol^{-1}, which is about 2/3 of the exit barrier). This type of dynamics is typical of H_2 elimination processes which are usually characterized by large exit barriers.

The C−C bond rupture in intermediate **4s** is accompanied by a strong repulsion between the CH_3 and HCS fragments, in which the carbon atom of the CH_3 rearranges from a tetrahedral to a trigonal hybridization in going from acetaldehyde to free methyl radical product. Clearly, the high fraction of energy in translation (from 42% to 58% in the different directions) reflects a nonstatistical decomposition of the complex **4s**, in which the partitioning of the total angular momentum dictates the dynamics.

5.3. Branching Ratios. The experimentally derived cross sections for the H, H_2, and HCS forming channels are in the ratio $\sigma_{H_2}/\sigma_H = 0.37$ and $\sigma_{HCS}/\sigma_H = 3.1$ at low E_c and $\sigma_{H_2}/\sigma_H = 0.34$ and $\sigma_{HCS}/\sigma_H = 4.5$ at high E_c. The slight increase of the HCS channel (the less exoergic channel) with increasing E_c is something than one would expect on energetic grounds.

We now compare these experimental estimates with the results of the statistical predictions. The RRKM calculations (see Tables 4 and 5) give a ratio $k_{H_2}/k_H = 1.80$ and $k_{HCS}/k_H = 3.80$ at low E_c, if addition is assumed to be the dominant initial attack of $S(^1D)$ to C_2H_4, while the ratios k_{H_2}/k_H and k_{HCS}/k_H become 0.45 and 3.80 in the case that insertion is the dominant attack of $S(^1D)$. At the high E_c the RRKM k_{H_2}/k_H and k_{HCS}/k_H

ratios are predicted to be 2.13 and 3.94 within the addition mechanism and 0.45 and 3.87 within the insertion mechanism. Comparing these predictions with the experimental estimates, in the assumption of a statistical description of this reaction one is led to the conclusion that insertion plays a significant role, being in this case the RRKM results for the H_2/H ratio (0.45) more in line with the experimental results (0.37−0.34). On the other end, as we have discussed, the relative importance of the H_2 channel with respect to the H channel may be underestimated in the experiment, which leaves room for both addition and insertion at play within a statistical behavior of the reaction. The ratio HCS/H of 3.80 (3.90 at high E_c) predicted by RRKM theory is instead in line with the experimental results of 3.1 (4.5 at high E_c), essentially unaffected by the relative role of insertion and addition, as discussed in section 4.4. Notably, the statistical calculations predict the CH_4 + CS channel to be minor (k_{CH_4}/k_H being predicted to be about 0.077 at low E_c and 0.074 at high E_c). Similarly, the H + CH_3CS channel with respect to the H + CH_2CHS channel, which is not surprising being the former significantly endoergic (see section 4.4).

The fact that RRKM calculations predict the HS channel to be the most important one (or comparable to the H channel if one assumes the transition state lies in the product valley) remains an open issue (see section 4.4). Unfortunately, although we have some evidence of reactive scattering signal at m/z = 33, we were unable to quantify its relative importance and therefore to discriminate between the two statistical predictions or whether the system is fully statistical.

5.4. Comparison with Thiirane Photodissociation. There have been a number of studies (both experimental and theoretical) on the thermal decomposition of thiirane[59] and especially on its photodissociation in a molecular beam at 193 nm using both electron-ionization[60] and VUV synchrotron radiation photoionization detection.[61] As thiirane is an important intermediate of the bimolecular $S(^1D) + C_2H_4$ reaction, the possible relevance of these unimolecular processes to our bimolecular studies is noted here. However, the observed dissociation dynamics of photoactivated thiirane to CH_2CHS + H and $C_2H_4 + S(^1D)$ is quite different from the dissociation of “chemically activated” thiirane on the ground state PES that we observe in our work. It should be noted, in fact, that the photodissociation of thiirane at 193 nm is very rapid, occurring on a time scale much shorter than a rotational period on excited singlet PESs.[59−61] In fact the HCS + CH_3 channel is not observed in the photodissociation studies indicating that excited thiirane does not have enough time to isomerize to ground-state thioacetaldehyde. An interesting aspect of the photodissociation work is the observation of the $S(^3P) + C_2H_4$ channel to a significant extent, which implies that ISC occurs quite readily in the system.

5.5. Comparison with the Reaction $O(^1D) + C_2H_4$. It is of some interest to compare the dynamics of the $S(^1D) + C_2H_4$ reaction with that of the related system $O(^1D) + C_2H_4$. It should be noted that in the reactions of ethene with S-atoms, only the channels leading to the molecular products $CH_2CS + H_2$ and CH_4 + CS are exoergic for $S(^3P)$, while those leading to radical products are strongly endoergic. In contrast, all the analogous reactions are exoergic for $O(^3P)$.[62,63] Recently, Lee and coworkers have investigated the reactions $O(^3P)/O(^1D)$ + ethene in CMB experiments with VUV photoionization detection.[64] In their work by using two distinct sources of O atoms they have sought to disentangle the reactions of $O(^3P)$ and $O(^1D)$ with C_2H_4. In particular they have focused on the relative reactivity of $O(^3P)$ and $O(^1D)$ for the channels leading to $H_2 + CH_2CO$ and CH_3 + HCO. Even though no direct information was provided about the relative importance of relaxation vs reaction for $O(^1D)$, from their work one could infer that physical quenching is not very important for $O(^1D)$. In general $^1D \rightarrow {}^3P$ quenching is expected to play a larger role in reactions with sulfur atoms than with oxygen atoms.

Notably, at the very low E_c of their experiment[64] ($E_c \sim 12$ kJ mol^{-1}) the CM angular and translational energy distributions for the H_2 and CH_3 forming channels from the $O(^1D) + C_2H_4$ reaction are rather in line with those determined in the present work for the corresponding H_2 and CH_3 channel from the $S(^1D) + C_2H_4$ reaction. Specifically the CM angular distributions are significantly polarized in both cases, but for $O(^1D)$ at $E_c \sim 12$ kJ mol^{-1} they are backward−forward symmetric, while for $S(^1D)$ at the much higher E_c of about 40 kJ mol^{-1} they are significantly forward biased. A shift from a backward−forward symmetry to a more forward scattering is what one would expect, within the osculating model for chemical reaction,[53] when rising the collision energy; in addition, a shorter lifetime of the intermediate complexes involving $S(^1D)$ (thiirane/CH_3CHS/CH_2CHSH) with respect to those involving $O(^1D)$ (CH_3CHO/CH_2CHOH) correlates well with their lower stability (with respect to reactants) of about 360 kJ mol^{-1} versus 650−600 kJ mol^{-1}. Finally, it is worth noting that the H channel has not been observed in the $O(^1D)$ reaction,[64] while it is quite significant for the $S(^1D)$ reaction. It will be interesting in the future to examine comparatively in detail these two related reactions, both experimentally and theoretically, to assess the relative role of ISC in the two cases.

6. Conclusion

We have reported a combined kinetics and crossed-beam dynamical study of the $S(^1D) + C_2H_4$ reaction. The interpretation of the experimental results has been assisted by high-level electronic structure calculations of the relevant potential energy surfaces and by statistical RRKM calculations of the reaction branching ratios. The low temperature kinetics experiments indicate that the reaction $S(^1D) + C_2H_4$ remains rapid down to the very low temperature of 23 K, occurring without any entrance barrier on the minimum energy path leading from reactants to products. This is corroborated by the theoretical calculations of the singlet C_2H_4S PES which did not find any appreciable reaction barrier to addition of $S(^1D)$ to the ethene molecule forming an initial thiirane stable intermediate or to insertion into a CH bond forming ethenethiol or any nonsubmerged barriers[65] to subsequent products. From laboratory angular and TOF distributions at different product masses and two different collision energies, three competing reaction channels leading to H + CH_2CHS (thiovinoxy), H_2 + CH_2CS (thioketene), and CH_3 + HCS (thioformyl) have been unambiguously identified and their dynamics characterized. From the derived CM product angular and translational energy distributions the reaction micromechanism, the product energy partitioning, and the relative ratio of cross sections for these competing reaction channels have been obtained. The relative ratio of cross sections did not vary significantly with collision energy. A hint of also HS + C_2H_3 (vinyl) formation has been obtained, but it could not be quantified because of experimental difficulties.

According to the experimental results and electronic structure calculations, the micromechanism of the $S(^1D) + C_2H_4$ reaction sees the addition, without any barrier, of the $S(^1D)$ atom to the double bond of the ethene molecule forming an internally excited thiirane intermediate which can undergo ring-opening and three-center H_2 elimination to thioketene (CH_2CS) + H_2 or, more readily, isomerize to slightly more stable thioacetaldehyde (CH_3CHS), which can undergo C−C bond cleavage to CH_3 + HCS and isomerization to vinylthiol (CH_2CHSH). Thiirane can also isomerize directly to vinylthiol through a somewhat higher barrier; vinylthiol, which can also be formed by direct insertion of $S(^1D)$ into one of the CH bonds, can in turn undergo C−H bond rupture to thiovinoxy (CH_2CHS) + H. While experimentally formation of HCS + CH_3 is found to be the most abundant channel (relative cross section 3.1−4.5), followed by H + CH_2CHS (1.0) and H_2 + CH_2CS (0.35), the variational RRKM predictions on one side corroborate semiquantitatively this trend, but on the other indicate HS + C_2H_3 (the least exoergic channel), originating from decomposition of vinylthiol, as the most abundant channel (branching ratio 0.76 at low E_c, see Table 5) with the H channel being minor (0.037). Notably, RRKM calculations which assume a transition state lying far in the product valley give however a HS/H ratio near unity. Clearly further experimental work is needed to clarify the relative importance of the HS + C_2H_3 channel in the $S(^1D)$ + C_2H_4 reaction.

These studies offer considerable promise for further dynamical investigations of other sulfur atom reactions of particular relevance to combustion and atmospheric chemistry.

Acknowledgment. We acknowledge financial support from the Italian MIUR (Ministero Istruzione Università Ricerca) under projects PRIN (2007H9S8SW_004 and 2007WLBXX9_004). This work has also been supported by the European Union Marie-Curie human resources and mobility programme under Contract MCRTN-CT-2004-512302, Molecular Universe. The Rennes team also acknowledges support from the French Agence Nationale de Recherche, Programme Blanc “Cold reactions of neutral species, CRNS”. D.S. thanks Alexander Mebel for useful suggestions on RRKM calculations. Finally, P.C. and S.D.L.P. acknowledge the Galileo Programme 2008/2009 between Perugia and Rennes.

References and Notes

(1) (a) Petherbridge, J. R.; May, P. W.; Shallcross, D. E.; Harvey, J. N.; Fuge, G. M.; Rosser, K. N.; Ashfold, M. N. R. *Diamond Relat. Mater.* **2003**, *12*, 2178. (b) Petherbridge, J. R.; May, P. W.; Fuge, G. M.; Rosser, K. N.; Ashfold, M. N. R. *Diamond Relat. Mater.* **2002**, *11*, 301.

(2) Morell, G.; Gonzalez-Berrýos, A.; Weiner, B. R.; Gupta, S. *J. Mater. Sci.: Mater. Electron.* **2006**, *17*, 443. Haubner, R.; Sommer, D. *Diamond Relat. Mater.* **2003**, *12*, 298.

(3) Nishitani-Gamo, M.; Yasu, E.; Xiao, C. Y.; Kikuchi, Y.; Ushizawa, K.; Sakaguchi, I.; Suzuki, T.; Ando, T. *Diamond Relat. Mater.* **2000**, *9*, 941.

(4) Schofield, K. *Combust. Flame* **2001**, *124*, 137.

(5) Bates, T. S.; Lamb, B. K.; Guenther, A.; Dignon, J.; Stoiber, R. E. *J. Atmos. Chem.* **1992**, *14*, 315.

(6) Wakelam, V.; Ceccarelli, C.; Castets, A.; Lefloch, B.; Loinard, L.; Faure, A.; Schneider, N.; Benayoun, J. J. *Astron. Astrophys.* **2005**, *437*, 149–158. Wakelam, V.; Caselli, R.; Ceccarelli, C.; Herbst, E.; Castets, A. *Astron. Astrophys.* **2004**, *422*, 159–169. Wakelam, V.; Castets, A.; Ceccarelli, C.; Lefloch, B.; Caux, E.; Pagani, L. *Astron. Astrophys.* **2004**, *413*, 609–622.

(7) Yamada, M.; Osamura, Y.; Kaiser, R. I. *Astronom. Astrophys.* **2002**, *395*, 1031.

(8) Petrie, S. *Mon. Not. R. Astron. Soc.* **1996**, *281*, 666.

(9) Dello Russo, N.; DiSanti, M. A.; Mumma, M. J.; Magee-Sauer, K.; Rettig, T. W. *Icarus* **1998**, *135*, 377.

(10) See, for instance: Krasnopolsky, V. A. *Icarus* **2007**, *191*, 25.

(11) See, for instance: Liu, K.; Han, W.; Pan, W.-P.; Riley, J. T. *J. Hazard. Mater.* **2001**, *B84*, 175. Ristovski, Z. D.; Jayaratne, E. R.; Lim, M.; Ayoko, G. A.; Morawska, L. *Environ. Sci. Technol.* **2006**, *40*, 1314.

(12) Strausz, O. P.; Gunning, H. E *J. Am. Chem. Soc.* **1962**, *84*, 4080. Sidhu, K. S.; Lown, E. M.; Strausz, O. P.; Gunning, H. E. *J. Am. Chem. Soc.* **1966**, *88*, 254.

(13) Lown, E. M.; Sandhu, H. S.; Gunning, H. E.; Strausz, O. P. *J. Am. Chem. Soc.* **1968**, *90*, 7164. Strausz, O. P.; Gunning, H. E.; Denes, A. S.; Csizmadia, I. G. *J. Am. Chem. Soc.* **1972**, *94*, 8317. Breckenridge, W. H.; Taube, H. *J. Chem. Phys.* **1970**, *53*, 1750. See also more recent work: Lee, J. H.; Tang, I. N. *J. Chem. Phys.* **1981**, *75*, 137. Tsuchiya, K.; Yamashita, K.; Miyoshi, A.; Matsui, H. *J. Phys. Chem.* **1996**, *100*, 17202. Lu, C.-W.; Wu, Y.-J.; Lee, Y.-P.; Zhu, R. S.; Lin, M. C. *J. Chem. Phys.* **2006**, *125*, 164329.

(14) Hoffmann, R.; Wan, C. C.; Neagu, V. *Mol. Phys.* **1970**, *19*, 113.

(15) McKee, M. L. *J. Am. Chem. Soc.* **1986**, *108*, 5059, and references therein.

(16) Schofield, K. *J. Phys. Chem. Ref. Data* **1979**, *8*, 723.

(17) Black, G.; Jusinski, L. E. *J. Chem. Phys.* **1985**, *82*, 789.

(18) Kjellström, E *J. Atm. Chem.* **1998**, *29*, 1951.

(19) van Veen, N.; Brewer, P.; Bershon, R. *J. Chem. Phys.* **1983**, *79*, 4295. Katayanagi, H.; Mo, Y.; Suzuki, T. *Chem. Phys. Lett.* **1995**, *217*, 571. Kim, M. H.; Li, W.; Lee, S. K.; Suits, A. G. *Can. J. Chem.* **2004**, *82*, 880.

(20) Halmer, M. M.; Schmincke, H.-U.; Graf, H.-F. *J. Volcanol. Geotherm. Res.* **2002**, *115*, 511.

(21) Cook, P. A.; Langford, S. R.; Dixon, R. N.; Ashfold, M. N. R. *J. Chem. Phys.* **2001**, *114*, 1672.

(22) Lee, S.-H.; Liu, K. *Chem. Phys. Lett.* **1998**, *290*, 323. Lee, S.-H.; Liu, K. *Appl. Phys. B: Lasers Opt.* **2000**, *71*, 627.

(23) Khachatrian, A.; Dagdigian, P. J. *J. Chem. Phys.* **2005**, *122*, 024303.

(24) Khachatrian, A.; Dagdigian, P. J. *Chem. Phys. Lett.* **2005**, *402*, 265.

(25) Leonori, F.; Petrucci, R.; Balucani, N.; Hickson, K. M.; Hamberg, M.; Geppert, W. D.; Casavecchia, P.; Rosi, M. *J. Phys. Chem. A* **2009**, *113*, 4330.

(26) Leonori, F.; Petrucci, R.; Balucani, N.; Casavecchia, P.; Rosi, M.; Berteloite, C.; Le Picard, S. D.; Canosa, A.; Sims, I. R. *Phys. Chem. Chem. Phys.* **2009**, *11*, 4701.

(27) Leonori, F.; Petrucci, R.; Wang, X.; Balucani, N.; Casavecchia, P.; Rosi, M.; Le Picard, S. D.; Berteloite, C.; Canosa, A.; Sims, I. R. In preparation.

(28) Black, G. *J. Chem. Phys.* **1986**, *84*, 1345.

(29) Canosa, A; Goulay, F.; Sims, I. R.; Rowe, B. R. In *Low Temperatures and Cold Molecules*; Smith, I. W. M. Ed.; World Scientific: Singapore, 2008.

(30) Sims, I. R.; Queffelec, J. L.; Defrance, A.; Rebrion-Rowe, C.; Travers, D.; Bocherel, P.; Rowe, B. R.; Smith, I. W. M. *J. Chem. Phys.* **1994**, *100*, 4229.

(31) Qi, F.; Sheng, L.; Ahmed, M.; Peterka, D. S.; Baer, T. *Chem. Phys. Lett.* **2002**, *357*, 204.

(32) Kitsopoulos, T. N.; Gebhardt, C. R.; Rakitzis, T. P. *J. Chem. Phys.* **2001**, *115*, 9727.

(33) Berteloite, C.; Le Picard, S. D.; Canosa, A.; Sims, I. R. 2009, manuscript in preparation.

(34) Hilbig, R.; Wallenstein, R. *IEEE J. Quantum Electron.* **1983**, *19*, 194.

(35) Chastaing, D.; Le Picard, S. D.; Sims, I. R. *J. Chem. Phys.* **2000**, *112*, 8466.

(36) Balucani, N.; Capozza, G.; Leonori, F.; Segoloni, E.; Casavecchia, P. *Int. Rev. Phys. Chem.* **2006**, *25*, 109.

(37) Alagia, M.; Balucani, N.; Casavecchia, P.; Stranges, D.; Volpi, G. G. *J. Chem. Soc., Faraday Trans.* **1995**, *91*, 575.

(38) Sibener, S. J.; Buss, R. J.; Ng, C.-Y.; Lee, Y. T. *Rev. Sci. Instrum.* **1980**, *51*, 167.

(39) Alagia, M.; Aquilanti, V.; Ascenzi, D.; Balucani, N.; Cappelletti, D.; Cartechini, L.; Casavecchia, P.; Pirani, F.; Sanchini, G.; Volpi, G. G. *Isr. J. Chem.* **1997**, *37*, 329.

(40) (a) Becke, A. D. *J. Phys. Chem.* **1993**, *98*, 5648. (b) Stephens, P. J.; Devlin, F. J.; Chablowski, C. F.; Frisch, M. J. *J. Phys. Chem.* **1994**, *98*, 11623.

(41) (a) Dunning, T. H., Jr. *J. Chem. Phys.* **1989**, *90*, 1007. (b) Woon, D. E.; Dunning, T. H., Jr. *J. Chem. Phys.* **1993**, *98*, 1358. (c) Kendall, R. A.; Dunning, T. H., Jr.; Harrison, R. J. *J. Chem. Phys.* **1992**, *96*, 6796.

(42) Bauschlicher, C. W., Jr.; Partridge, H. *Chem. Phys. Lett.* **1995**, *240*, 533.

(43) Martin, J. M. L.; Uzan, O. *Chem. Phys. Lett.* **1998**, *282*, 16.

(44) (a) Gonzales, C.; Schlegel, H. B. *J. Chem. Phys.* **1989**, *90*, 2154. (b) *J. Phys. Chem.* **1990**, *94*, 5523.

(45) (a) Bartlett, R. J. *Annu. Rev. Phys. Chem.* **1981**, *32*, 359. (b) Raghavachari, K.; Trucks, G. W.; Pople, J. A.; Head-Gordon, M. *Chem. Phys. Lett.* **1989**, *157*, 479. (c) Olsen, J.; Jorgensen, P.; Koch, H.; Balkova, A.; Bartlett, R. J. *J. Chem. Phys.* **1996**, *104*, 8007.

(46) Shiina, H.; Miyoshi, A.; Matsui, H. *J. Phys. Chem. A* **1998**, *102*, 3556.

(47) (a) Martin, J. M. L.; de Oliveira, G. *J. Chem. Phys.* **1999**, *111*, 1843. (b) Parthiban, S.; Martin, J. M. L. *J. Chem. Phys.* **2001**, *114*, 6014.

(48) Frisch, M. J.; Trucks, G. W.; Schlegel, H. B.; Scuseria, G. E.; Robb, M. A.; Cheeseman, J. R.; Montgomery, J. A., Jr.; Vreven, T.; Kudin, K. N.; Burant, J. C.; Millam, J. M.; Iyengar, S. S.; Tomasi, J.; Barone, V.;

Mennucci, B.; Cossi, M.; Scalmani, G.; Rega, N.; Petersson, G. A.; Nakatsuji, H.; Hada, M.; Ehara, M.; Toyota, K.; Fukuda, R.; Hasegawa, J.; Ishida, M.; Nakajima, T.; Honda, Y.; Kitao, O.; Nakai, H.; Klene, M.; Li, X.; Knox, J. E.; Hratchian, H. P.; Cross, J. B.; Bakken, V.; Adamo, C.; Jaramillo, J.; Gomperts, R.; Stratmann, R. E.; Yazyev, O.; Austin, A. J.; Cammi, R.; Pomelli, C.; Ochterski, J. W.; Ayala, P. Y.; Morokuma, K.; Voth, G. A.; Salvador, P.; Dannenberg, J. J.; Zakrzewski, V. G.; Dapprich, S.; Daniels, A. D.; Strain, M. C.; Farkas, O.; Malick, D. K.; Rabuck, A. D.; Raghavachari, K.; Foresman, J. B.; Ortiz, J. V.; Cui, Q.; Baboul, A. G.; Clifford, S.; Cioslowski, J.; Stefanov, B. B.; Liu, G.; Liashenko, A.; Piskorz, P.; Komaromi, I.; Martin, R. L.; Fox, D. J.; Keith, T.; Al-Laham, M. A.; Peng, C. Y.; Nanayakkara, A.; Challacombe, M.; Gill, P. M. W.; Johnson, B.; Chen, W.; Wong, M. W.; Gonzalez, C.; Pople, J. A. *Gaussian 03, Revision D.01*; Gaussian, Inc.: Wallingford, CT, 2004.

(49) (a) Flükiger, P.; Lüthi, H. P.; Portmann, S.; Weber, J. *MOLEKEL 4.3*; Swiss Center for Scientific Computing: Manno, Switzerland, 2000−2002. (b) Portmann, S.; Lüthi, H. P. *Chimia* **2000**, *54*, 766.

(50) Balucani, N.; Bergeat, A.; Cartechini, L., Volpi, G. G.; Casavecchia, P.; Skouteris, D.; Rosi, M. *J. Phys. Chem. A* **2009**, in press. Published on July 30, 2009 on http://pubs.acs.org | doi:, 10.1021/jp904302g.

(51) Gilbert, R. G.; Smith, S. C. *Theory of unimolecular and recombination reactions*; Blackwell Scientific Publications: Oxford, U.K., 1990. Baer, T.; Hase, W. L. *Unimolecular Reaction Dynamics: Theory and Experiments*, Oxford University Press: New York, 1996.

(52) Klippenstein, S. J. *J. Chem. Phys.* **1992**, *96*, 367.

(53) Fisk, G. A.; Mc Donald, J. D.; Herschbach, D. R. *Discuss. Faraday Soc.* **1967**, *44*, 228. Miller, W. B.; Safron, S. A.; Herschbach, D. R. *Discuss. Faraday Soc.* **1967**, *44*, 108. *J. Chem. Phys.* **1972**, *56*, 3581.

(54) Chin, W. S.; Ek, B. W.; Mok, C. Y.; Huang, H. H. *J. Chem. Soc., Perkin Trans. 2* **1994**, 883.

(55) (a) Qi, F.; Sorkhabi, O.; Suits, A. G.; Chien, S.-H.; Li, W.-K. *J. Am. Chem. Soc.* **2001**, *123*, 148. (b) Ding, W.-J.; Fang, W.-H.; Liu, R.-Z. *J. Mol. Struct.: THEOCHEM* **2004**, *682*, 29.

(56) Woon, D. E. *J. Phys. Chem. A* **2007**, *111*, 11249.

(57) Gunning, H. E; Strausz, O. P. *Adv. Photochem.* **1966**, *4*, 143. Fowles, M.; de Sorgo, M.; Yarwood, A. J.; Strausz, O. P.; Gunning, H. E *J. Am. Chem. Soc.* **1967**, *89*, 1352.

(58) Davis, D. D.; Klemm, R. B.; Braun, W.; Pilling, M. *Int. J. Chem. Kinet.* **1972**, *4*, 383.

(59) Chin, W. S.; Ek, B. W.; Mok, C. Y.; Huang, H. H. *J. Chem. Soc., Perkin Trans. 2* **1994**, 883.

(60) Kim, H. L.; Satyapal, S.; Brewer, P.; Bersohn, R *J. Chem. Phys.* **1989**, *91*, 1047. Felder, P.; Wannenmacher, E. A. J.; Wiedmer, I.; Huber, J. R. *J. Phys. Chem.* **1992**, *96*, 4470.

(61) Qi, F.; Sorkhabi, O.; Suits, A. G.; Chien, S.-H.; Li, W.-K. *J. Am. Chem. Soc.* **2001**, *123*, 148. Suits, A. G.; Qi, F. *J. Electron Spectrosc. Relat. Phenom.* **2001**, *119*, 127.

(62) Casavecchia, P.; Capozza, G.; Segoloni, E.; Leonori, F.; Balucani, N.; Volpi, G. G. *J. Phys. Chem. A* **2005**, *109*, 3527.

(63) Nguyen, T. L.; Vereecken, L.; Peeters, J. *J. Phys. Chem. A* **2006**, *110*, 6696.

(64) Lee, S.-H.; Chen, W.-K.; Huang, W.-J. *J. Chem. Phys.* **2008**, *130*, 054301.

(65) Sabbah, H.; Biennier, L.; Sims, I. R.; Georgievskii, Y.; Klippenstein, S. J.; Smith, I. W. M. *Science* **2007**, *317*, 102.

JP906299V